

Discrete-state Continuous-time Diffusion for Graph Generation

Zhe Xu* Ruizhong Qiu* Yuzhong Chen† Huiyuan Chen† Xiran Fan† Menghai Pan†

Zhichen Zeng*

Mahashweta Das†

Hanghang Tong*

Abstract

Graph is a prevalent discrete data structure, whose generation has wide applications such as drug discovery and circuit design. Diffusion generative models, as an emerging research focus, have been applied to graph generation tasks. Overall, according to the space of *states* and *time* steps, diffusion generative models can be categorized into discrete-/continuous-state discrete-/continuous-time fashions. In this paper, we formulate the graph diffusion generation in a discrete-state continuous-time setting, which has never been studied in previous graph diffusion models. The rationale of such a formulation is to preserve the discrete nature of graph-structured data and meanwhile provide flexible sampling trade-offs between sample quality and efficiency. Analysis shows that our training objective is closely related to the generation quality and our proposed generation framework enjoys ideal invariant/equivariant properties concerning the permutation of node ordering. Our proposed model shows competitive empirical performance against state-of-the-art graph generation solutions on various benchmarks and at the same time can flexibly trade off the generation quality and efficiency in the sampling phase.

1 Introduction

Graph generation has been studied for a long time with broad applications, based on either the one-shot (i.e., one-step) [42, 32, 48, 43, 61, 27] or auto-regressive generation paradigm [68, 24, 35, 44]. The former generates all the graph components at once and the latter does that sequentially. A recent trend of applying diffusion generative models [57, 18, 59] to graph generation tasks attracts increasing attentions because of its excellent performance and solid theoretical foundation. In this paper, we follow the one-shot generation paradigm, the same as most graph diffusion generative models.

Some earlier attempts at graph diffusion models treat the graph data in a continuous state space by viewing the graph topology and features as continuous variables [48]. Such a formulation departs from the discrete nature of graph-structured data; e.g., topological sparsity is lost and the discretization in the generation process requires extra hyper-parameters. DiGress [62] is the first work applying

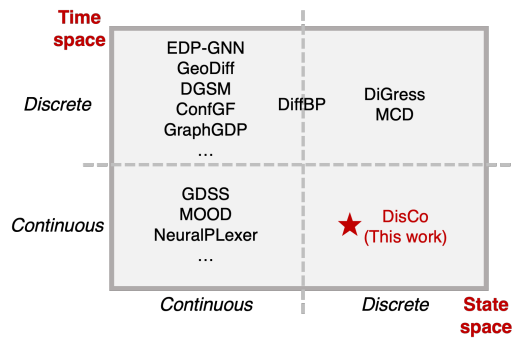


Figure 1: A taxonomy of graph diffusion models.

*University of Illinois Urbana-Champaign, corresponding: zhexu3@illinois.edu

†Visa Research

discrete-state diffusion models to graph generation tasks and is the current state-of-the-art graph diffusion generative model. However, DiGress is defined in the discrete time space whose generation is inflexible. This is because, its number of sampling steps must match the number of forward diffusion steps, which is a fixed hyperparameter after the model finishes training. A unique advantage of the continuous-time diffusion models [59, 27] lies in their flexible sampling process, and its simulation complexity is proportional to the number of sampling steps, which is determined by the step size of various numerical approaches (e.g., τ -leaping [14, 7, 60]) and decoupled from the training of models. Thus, a discrete-state continuous-time diffusion model is highly desirable for graph generation tasks.

Driven by the recent advance of continuous-time Markov Chain (CTMC)-based diffusion generative model [7], we incorporate the ideas of CTMC into the corruption and denoising of graph data and propose the first discrete-state continuous-time graph diffusion generative model. It shares the same advantages as DiGress by preserving the discrete nature of graph data and meanwhile overcomes the drawback of the nonadjustable sampling process in DiGress. This Discrete-state Continuous-time graph diffusion model is named DISCO.

DISCO bears several desirable properties and advantages. First, despite its simplicity, the training objective has a rigorously proved connection to the sampling error. Second, its formulation includes a parametric graph-to-graph mapping, named backbone model, whose input-output architecture is shared between DISCO and DiGress. Therefore, the graph transformer (GT)-based backbone model [46] from DiGress can be seamlessly plugged into DISCO. Third, a concise message-passing neural network backbone model is explored with DISCO, which is much simpler than the GT backbone and performs competitively empirically. Last but not least, our analyses show that the forward and reverse diffusion process in DISCO can retain the permutation-equivariant/invariant properties for both its training loss and sampling distribution; they are critical and practical inductive biases on graph data.

Our comprehensive experiments on plain and molecule graphs show that DISCO can obtain competitive or superior performance against state-of-the-art graph generative models and provide additional sampling flexibility. Our main contributions are summarized as follows.

- **Model.** We propose the first discrete-state continuous-time graph diffusion model, DISCO. Also, we utilize the successful graph-to-graph neural network architecture from DiGress and further explore a new lightweight backbone model with decent efficacy.
- **Analysis.** Our analysis reveals (1) the key connection between the training loss and the approximation error (Theorem 3.3) and (2) invariant/equivariant properties of DISCO in terms of the permutation of nodes (Theorems 3.8 and 3.9).
- **Experiment.** Extensive experiments evaluate the empirical performance of DISCO.

2 Preliminaries

2.1 Discrete-State Continuous-time Diffusion Models

A D -dimensional discrete state space is represented as $\mathcal{X} = \{1, \dots, C\}^D$. A continuous-time Markov Chain (CTMC) $\{\mathbf{x}_t = [x_t^1, \dots, x_t^D]\}_{t \in [0, T]}$ is characterized by its (time-dependent) rate matrix $\mathbf{R}_t \in \mathbb{R}^{|\mathcal{X}| \times |\mathcal{X}|}$. Here \mathbf{x}_t is the state at the time step t . The transition probability $q_{t|s}$ between the time interval s to t satisfies the Kolmogorov forward equation, for $s < t$,

$$\frac{d}{dt} q_{t|s}(\mathbf{x}_t | \mathbf{x}_s) = \sum_{\xi \in \mathcal{X}} q_{t|s}(\xi | \mathbf{x}_s) \mathbf{R}_t(\xi, \mathbf{x}_t), \quad (1)$$

The marginal distribution can be represented as

$$q_t(\mathbf{x}_t) = \sum_{\mathbf{x}_0 \in \mathcal{X}} q_{t|0}(\mathbf{x}_t | \mathbf{x}_0) \pi_{\text{data}}(\mathbf{x}_0), \quad (2)$$

where $\pi_{\text{data}}(\mathbf{x}_0)$ is the data distribution. If the CTMC is defined in time interval $[0, T]$ and if the rate matrix \mathbf{R}_t is well-designed, the final distribution $q_T(\mathbf{x}_T)$ can be close to a tractable reference distribution $\pi_{\text{ref}}(\mathbf{x}_T)$, e.g., uniform distribution. We notate the reverse stochastic process as $\tilde{\mathbf{x}}_t =$

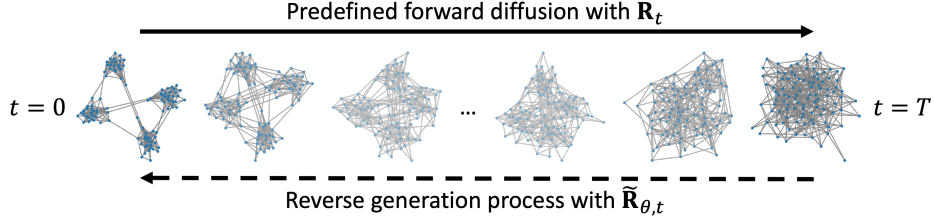


Figure 2: An overview of discrete-state continuous-time graph diffusion. A transition can happen at any time in $[0, T]$.

\mathbf{x}_{T-t} , A well-known fact (e.g., Section 5.9 in [53]) is that the reverse process $\{\tilde{\mathbf{x}}_t\}_{t \in [0, T]}$ is also a CTMC. It is characterized by the reverse rate matrix defined as

$$\tilde{\mathbf{R}}_t(\mathbf{x}, \mathbf{y}) = \frac{q(\mathbf{y})}{q(\mathbf{x})} \mathbf{R}_t(\mathbf{y}, \mathbf{x}). \quad (3)$$

The goal of the CTMC-based diffusion models is an accurate estimation of the reverse rate matrix $\tilde{\mathbf{R}}_t$ so that new data can be generated by sampling the reference distribution π_{ref} and then simulating the reverse CTMC [12, 13, 14, 1]. However, the complexity of the rate matrix is prohibitively high because there are C^D possible states. A reasonable simplification is to factorize the process over dimensions [7, 60, 62, 2]. Specifically, the forward process is factorized as $q_{t|s}(\mathbf{x}_t | \mathbf{x}_s) = \prod_{d=1}^D q_{t|s}(x_t^d | x_s^d)$, for $s < t$. Then, the forward diffusion of each dimension is independent and is governed by dimension-specific forward rate matrices $\{\mathbf{R}_t^d\}_{d=1}^D$. With such a factorization, the goal is to estimate the dimension-specific reverse rate matrices $\{\tilde{\mathbf{R}}_t^d\}_{d=1}^D$.

The reverse rate of one dimension is represented as $\tilde{\mathbf{R}}_t^d(x^d, y^d) = \sum_{x_0^d} \mathbf{R}_t^d(y^d, x^d) \frac{q_{t|0}(y^d | x_0^d)}{q_{t|0}(x^d | x_0^d)} q_{0|t}(x_0^d | \mathbf{x})$. Campbell et al. [7] estimate $q_{0|t}(x_0^d | \mathbf{x})$ via a neural network p_θ such that $p_\theta(x_0^d | \mathbf{x}, t) \approx q_{0|t}(x_0^d | \mathbf{x})$; Sun et al. [60] propose another singleton conditional distribution-based objective $\frac{p_\theta(y^d | \mathbf{x}^{\setminus d}, t)}{p_\theta(x^d | \mathbf{x}^{\setminus d}, t)} \approx \frac{q(y^d | \mathbf{x}^{\setminus d})}{q(x^d | \mathbf{x}^{\setminus d})}$ whose rationale is Brook's Lemma [4, 41].

2.2 Graph Generation and Notations

We study the generation of graphs with *categorical* node and edge attributes. A graph with n nodes is represented by its edge type matrix and node type vector: $\mathcal{G} = (\mathbf{E}, \mathbf{F})$, where $\mathbf{E} = \{e^{(i,j)}\}_{i,j \in \mathbb{N}_{\leq n}^+} \in \{1, \dots, a, a+1\}^{n \times n}$, $\mathbf{F} = \{f^i\}_{i \in \mathbb{N}_{\leq n}^+} \in \{1, \dots, b\}^n$, a is the number of edge types, and b is the number of node types. Notably, the absence of an edge is viewed as a special edge type, so that in total there are $(a+1)$ edge types. The problem we study is defined as follows.

Problem 2.1. Graph Generation

Given: N graphs $\{\mathcal{G}^i\}_{i \in \mathbb{N}_{\leq N}^+}$ from an inaccessible graph data distribution \mathfrak{G} .

Find: M generated graphs $\{\mathcal{G}^i\}_{i \in \mathbb{N}_{\leq M}^+}$ from the distribution \mathfrak{G} .

3 Method

This section presents the proposed discrete-state continuous-time graph diffusion model, DISCO. An overview of DISCO is presented in Figure 2. Section 3.1 introduces the necessity to factorize the diffusion process and Section 3.2 details the forward process. Our training objective and its connection to sampling are introduced in Sections 3.3 and 3.4, respectively. Last but not least, a specific neural architecture of the graph-to-graph backbone model and its properties regarding the permutation of node ordering are introduced in Sections 3.5 and 3.6, respectively.

All proofs are in Appendix.

3.1 Factorized Discrete Graph Diffusion Process

The number of possible states of an n -node graph is $(a + 1)^{n^2} \times b^n$ which is intractably large. Thus, we follow existing discrete models [2, 7, 60, 62] and formulate the forward processes on every node/edge to be independent. Mathematically, the forward diffusion process for $s < t$ is factorized as

$$q_{t|s}(\mathcal{G}_t|\mathcal{G}_s) = \prod_{i,j=1}^n q_{t|s}(e_t^{(i,j)}|e_s^{(i,j)}) \prod_{i=1}^n q_{t|s}(f_t^i|f_s^i) \quad (4)$$

where the edge type transition probabilities $\{q_{t|s}(e_t^{(i,j)}|e_s^{(i,j)})\}_{i,j \in \mathbb{N}_{\leq n}^+}$ and node type transition probabilities $\{q_{t|s}(f_t^i|f_s^i)\}_{i \in \mathbb{N}_{\leq n}^+}$ are characterized by their forward rate matrices $\{\mathbf{R}_t^{(i,j)}\}_{i,j \in \mathbb{N}_{\leq n}^+}$ and $\{\mathbf{R}_t^i\}_{i \in \mathbb{N}_{\leq n}^+}$, respectively. The forward processes, i.e., the forward rate matrices in our context, are predefined, which will be introduced in Section 3.2. Given the factorization of forward transition probability in Eq. (4), a question is raised: *what is the corresponding factorization of the forward rate matrix (\mathbf{R}_t) and the reverse rate matrix ($\tilde{\mathbf{R}}_t$)?* Remark 3.1 shows such a factorization.

Remark 3.1. (Factorization of rate matrices, extended from Proposition 3 of [7]) Given the factorized forward process Eq. (4), the overall rate matrices are factorized as

$$\mathbf{R}_t(\bar{\mathcal{G}}, \mathcal{G}) = \sum_i A_t^i + \sum_{i,j} B_t^{(i,j)} \quad (5)$$

$$\tilde{\mathbf{R}}_t(\mathcal{G}, \bar{\mathcal{G}}) = \sum_i A_t^i \sum_{f_0^i} \frac{q_{t|0}(\bar{f}^i|f_0^i)}{q_{t|0}(f^i|f_0^i)} q_{0|t}(f_0^i|\mathcal{G}) + \sum_{i,j} B_t^{(i,j)} \sum_{e_0^{(i,j)}} \frac{q_{t|0}(\bar{e}^{(i,j)}|e_0^{(i,j)})}{q_{t|0}(e^{(i,j)}|e_0^{(i,j)})} q_{0|t}(e_0^{(i,j)}|\mathcal{G}), \quad (6)$$

where $A_t^i = \mathbf{R}_t^i(\bar{f}^i, f^i) \delta_{\bar{\mathcal{G}} \setminus \bar{f}^i, \mathcal{G} \setminus f^i}$, $B_t^{(i,j)} = \mathbf{R}_t^{(i,j)}(\bar{e}^{(i,j)}, e^{(i,j)}) \delta_{\bar{\mathcal{G}} \setminus \bar{e}^{(i,j)}, \mathcal{G} \setminus e^{(i,j)}}$, the operator $\delta_{\bar{\mathcal{G}} \setminus \bar{f}^i, \mathcal{G} \setminus f^i}$ (or $\delta_{\bar{\mathcal{G}} \setminus \bar{e}^{(i,j)}, \mathcal{G} \setminus e^{(i,j)}}$) checks whether two graphs $\bar{\mathcal{G}}$ and \mathcal{G} are exactly the same except for node i (or the edge between nodes i and j).

Note that this factorization itself is not our contribution but a necessary part of our framework, so we mention it here for completeness. Its full derivation is in Appendix - Section A. Next, we detail the design of forward rate matrices and the estimation of reverse rate matrices.

3.2 Forward Process

A proper choice of the forward rate matrices $\{\mathbf{R}_t^{(i,j)}\}_{i,j \in \mathbb{N}_{\leq n}^+}$ and $\{\mathbf{R}_t^i\}_{i \in \mathbb{N}_{\leq n}^+}$ is important because (1) the probability distributions of node and edge types, $\{q(f_t^i)\}_{i \in \mathbb{N}_{\leq n}^+}$ and $\{q(e_t^{(i,j)})\}_{i,j \in \mathbb{N}_{\leq n}^+}$, should converge to their reference distributions within $[0, T]$ and (2) the reference distributions should be easy to sample (e.g., uniform distribution). We follow [7] to formulate $\mathbf{R}_t^{(i,j)} = \beta(t) \mathbf{R}_e^{(i,j)}$, $\forall i, j$ and $\mathbf{R}_t^i = \beta(t) \mathbf{R}_f^i$, $\forall i$, where $\beta(t)$ is a corruption schedule, $\{\mathbf{R}_e^{(i,j)}\}$ and $\{\mathbf{R}_f^i\}$ are the base rate matrices. For brevity, we set all the nodes/edges to share a common node/edge rate matrix, i.e., $\mathbf{R}_e^{(i,j)} = \mathbf{R}_e$ and $\mathbf{R}_f^i = \mathbf{R}_f$, $\forall i, j$. Then, the forward transition probability for all the nodes and edges are $q_{t|0}(f_t = v|f_0 = u) = (e^{\int_0^t \beta(s) \mathbf{R}_f ds})_{uv}$ and $q_{t|0}(e_t = v|e_0 = u) = (e^{\int_0^t \beta(s) \mathbf{R}_e ds})_{uv}$, respectively. We omit the superscript i (or (i, j)) because the transition probability is shared by all the nodes (or edges). The detailed derivation of the above analytic forward transition probability is provided in Appendix - Section B.

For categorical data, a reasonable reference distribution is a uniform distribution, i.e., $\pi_f = \frac{1}{b}$ for nodes and $\pi_e = \frac{1}{a+1}$ for edges. In addition, inspired by [62], we find that node and edge marginal distributions \mathbf{m}_f and \mathbf{m}_e are good choices as the reference distributions. Concretely, an empirical estimation of \mathbf{m}_f and \mathbf{m}_e is to count the number of node/edge types and normalize them. The following proposition shows how to design the rate matrices to guide the forward process to converge to uniform and marginal distributions.

Algorithm 1 Training of DISCO

- 1: Given a training graph $\mathcal{G}_0 = (\{f_0^i\}, \{e_0^{(i,j)}\})$
 - 2: Sample $t \sim \mathcal{U}_{(0,T)}$
 - 3: Sample \mathcal{G}_t based on transition probabilities $q_{t|0}(f_t = v | f_0 = u) = (e^{\int_0^t \beta(s) \mathbf{R}_f ds})_{uv}$ and $q_{t|0}(e_t = v | e_0 = u) = (e^{\int_0^t \beta(s) \mathbf{R}_e ds})_{uv}$, given $\mathcal{G}_0 = (\{f_0^i\}, \{e_0^{(i,j)}\})$
 - 4: Predict the clean graph $\hat{\mathcal{G}}_0 = (\{\hat{f}_0^i\}, \{\hat{e}_0^{(i,j)}\}) \leftarrow (\{p_{0|t}^\theta(f^i | \mathcal{G}_t)\}, \{p_{0|t}^\theta(e^{(i,j)} | \mathcal{G}_t)\})$, given \mathcal{G}_t
 - 5: Compute cross-entropy loss between \mathcal{G}_0 and $\hat{\mathcal{G}}_0$ based on Eq. (9) and update θ
-

Proposition 3.2. *The forward process for nodes and edges converges to uniform distributions if $\mathbf{R}_f = \mathbf{1}\mathbf{1}^\top - b\mathbf{I}$ and $\mathbf{R}_e = \mathbf{1}\mathbf{1}^\top - (a+1)\mathbf{I}$. The forward process for nodes and edges converges to marginal distributions \mathbf{m}_f and \mathbf{m}_e if $\mathbf{R}_f = \mathbf{1}\mathbf{m}_f^\top - \mathbf{I}$ and $\mathbf{R}_e = \mathbf{1}\mathbf{m}_e^\top - \mathbf{I}$. For both cases, $\mathbf{R}_e \in \mathbb{R}^{(a+1) \times (a+1)}$, $\mathbf{R}_f \in \mathbb{R}^{b \times b}$, $\mathbf{1}$ is an all-one column vector, and \mathbf{I} is an identity matrix.*

Regarding the selection of $\beta(t)$, we follow [18, 59, 7] and set $\beta(t) = \alpha\gamma^t \log(\gamma)$ for a smooth change of the rate matrix. α and γ are hyperparameters. Detailed settings are in Appendix F.3.

3.3 Parameterization and Optimization Objective

Next, we introduce the estimation and parameterization of the reverse process from its motivation. The reverse process is essentially determined by the reverse rate matrix $\tilde{\mathbf{R}}_t$ in Eq. (6), whose computation needs $q_{0|t}(f_0^i | \mathcal{G})$ and $q_{0|t}(e_0^{(i,j)} | \mathcal{G})$; they are expensive to estimate exactly because according to Bayes' rule, $p_t(\mathcal{G})$ is needed, whose computation needs to enumerate all the given graphs: $p_t(\mathcal{G}) = \sum_{\mathcal{G}_0} q_{t|0}(\mathcal{G} | \mathcal{G}_0) \pi_{\text{data}}(\mathcal{G}_0)$.

Thus, we propose parameterizing the reverse transition probabilities via a neural network θ whose specific architecture is introduced in Section 3.5. The terms $\{q_{0|t}(f_0^i | \mathcal{G})\}_{i \in \mathbb{N}_{\leq n}^+}$ and $\{q_{0|t}(e_0^{(i,j)} | \mathcal{G})\}_{i,j \in \mathbb{N}_{\leq n}^+}$ in Eq. (6) are replaced with the parameterized $\{p_{0|t}^\theta(f^i | \mathcal{G})\}_{i \in \mathbb{N}_{\leq n}^+}$ and $\{p_{0|t}^\theta(e^{(i,j)} | \mathcal{G})\}_{i,j \in \mathbb{N}_{\leq n}^+}$. Thus, a parameterized reverse rate matrix $\tilde{\mathbf{R}}_{\theta,t}(\mathcal{G}, \bar{\mathcal{G}})$ is represented as

$$\tilde{\mathbf{R}}_{\theta,t}(\mathcal{G}, \bar{\mathcal{G}}) = \sum_i \tilde{\mathbf{R}}_{\theta,t}^i(f^i, \bar{f}^i) + \sum_{i,j} \tilde{\mathbf{R}}_{\theta,t}^{(i,j)}(e^{(i,j)}, \bar{e}^{(i,j)}) \quad (7)$$

where $\tilde{\mathbf{R}}_{\theta,t}^i(f^i, \bar{f}^i) = A_t^i \sum_{f_0^i} \frac{q_{t|0}(\bar{f}^i | f_0^i)}{q_{t|0}(f^i | f_0^i)} p_{0|t}^\theta(f^i | \mathcal{G})$, $\tilde{\mathbf{R}}_{\theta,t}^{(i,j)}(e^{(i,j)}, \bar{e}^{(i,j)}) = B_t^{(i,j)} \sum_{e_0^{(i,j)}} \frac{q_{t|0}(\bar{e}^{(i,j)} | e_0^{(i,j)})}{q_{t|0}(e^{(i,j)} | e_0^{(i,j)})} p_{0|t}^\theta(e_0^{(i,j)} | \mathcal{G})$, and the remaining notations are the same as Eq. (6). Note that all the above terms $\{p_{0|t}^\theta(f^i | \mathcal{G})\}_{i \in \mathbb{N}_{\leq n}^+}$ and $\{p_{0|t}^\theta(e^{(i,j)} | \mathcal{G})\}_{i,j \in \mathbb{N}_{\leq n}^+}$ can be viewed together as a graph-to-graph mapping $\theta : \mathfrak{G} \rightarrow \mathfrak{G}$, whose input is the noisy graph \mathcal{G}_t and its output is the predicted clean graph probabilities, concretely, the node/edge type probabilities of all the nodes and edges.

Intuitively, the discrepancy between the groundtruth reverse rate matrix $\tilde{\mathbf{R}}_t$ (from Eq. (6)) and the parametric reverse rate matrix $\tilde{\mathbf{R}}_{\theta,t}$ should be small. Our following analysis (Theorem 3.3) establishes an upper bound of such a discrepancy, where the node and edge estimated probability vector (sum is 1) is notated as $\hat{f}_0^i = [p_{0|t}^\theta(f^i = 1 | \mathcal{G}_t), \dots, p_{0|t}^\theta(f^i = b | \mathcal{G}_t)]^\top \in [0, 1]^b$ and $\hat{e}_0^{(i,j)} = [p_{0|t}^\theta(e^{(i,j)} = 1 | \mathcal{G}_t), \dots, p_{0|t}^\theta(e^{(i,j)} = a+1 | \mathcal{G}_t)]^\top \in [0, 1]^{a+1}$.

Theorem 3.3 (Approximation error). *for $\mathcal{G} \neq \bar{\mathcal{G}}$*

$$\begin{aligned} \left| \tilde{\mathbf{R}}_t(\mathcal{G}, \bar{\mathcal{G}}) - \tilde{\mathbf{R}}_{\theta,t}(\mathcal{G}, \bar{\mathcal{G}}) \right|^2 &\leq C_t + C_t^{\text{node}} \mathbb{E}_{\mathcal{G}_0} q_{t|0}(\mathcal{G} | \mathcal{G}_0) \sum_i \mathcal{L}_{\text{CE}}(\text{One-Hot}(f_0^i), \hat{f}_0^i) \\ &\quad + C_t^{\text{edge}} \mathbb{E}_{\mathcal{G}_0} q_{t|0}(\mathcal{G} | \mathcal{G}_0) \sum_{i,j} \mathcal{L}_{\text{CE}}(\text{One-Hot}(e_0^{(i,j)}), \hat{e}_0^{(i,j)}) \end{aligned} \quad (8)$$

where C_t , C_t^{node} , and C_t^{edge} are constants independent on θ but dependent on t , \mathcal{G} , and $\bar{\mathcal{G}}$; One-Hot transforms f_0^i and $e_0^{(i,j)}$ into one-hot vectors.

The bound in Theorem 3.3 is tight, i.e., the right-hand side of Eq. (8) is 0, whenever $\hat{f}_0^i = q_{0|t}(f_0^i|\mathcal{G}_t), \forall i$ and $\hat{e}_0^{(i,j)} = q_{0|t}(e_0^{(i,j)}|\mathcal{G}_t), \forall i, j$. Guided by Theorem 3.3, we (1) take expectation over all the time t by sampling t from a uniform distribution and (2) simplify the right-hand side of Eq. (8) and use the unweighted cross-entropy (CE) loss as our training objective:

$$\min_{\theta} T \mathbb{E}_{t \sim \mathcal{U}(0, T)} \mathbb{E}_{\mathcal{G}_0} \mathbb{E}_{q_{t|0}(\mathcal{G}_t|\mathcal{G}_0)} \left[\sum_i \mathcal{L}_{\text{CE}}(\text{One-Hot}(f_0^i), \hat{f}_0^i) + \sum_{i,j} \mathcal{L}_{\text{CE}}(\text{One-Hot}(e_0^{(i,j)}), \hat{e}_0^{(i,j)}) \right] \quad (9)$$

A step-by-step training algorithm is presented in Algorithm 1. It is worth mentioning that the above CE loss has been used in some diffusion models (e.g., [2, 7]) but lacks a good motivation, especially in the continuous-time setting. Our analysis motivates it based on the rate matrix discrepancy, as a unique contribution of this paper.

3.4 Sampling Reverse Process

Given the parametric reverse rate matrix $\tilde{\mathbf{R}}_{\theta,t}(\mathcal{G}, \bar{\mathcal{G}})$, the graph generation process can be implemented by two steps: (1) sampling the reference distribution π_{ref} (i.e., π_f for nodes and π_e for edges) and (2) numerically simulating the CTMC from time T to 0.

The exact simulation of a CTMC based on its rate matrix has been studied for a long time, e.g., [12, 13, 1]. However, their simulation strategies only allow one transition (e.g., one edge/node type change) per step, which is highly inefficient for graphs as the number of nodes and edges is typically large; once a(n) node/edge is updated, $\tilde{\mathbf{R}}_{\theta,t}$ requires recomputation. A practical approximation is to assume $\tilde{\mathbf{R}}_{\theta,t}$ is fixed, during a time interval $[t - \tau, t]$, i.e., delaying the happening of transitions in $[t - \tau, t]$ and triggering them all together at the time $t - \tau$; this strategy is also known as τ -leaping [14, 7, 60]. DISCO adopts this sampling strategy.

We elaborate on τ -leaping for transitions of node types; the transitions of edge types are similar. The rate matrix of the i -th node is fixed as $\tilde{\mathbf{R}}_{\theta,t}^i(f^i, \bar{f}^i) = \mathbf{R}_t^i(\bar{f}^i, f^i) \sum_{f_0^i} \frac{q_{t|0}(\bar{f}^i|f_0^i)}{q_{t|0}(f^i|f_0^i)} p_{0|t}^\theta(f^i|\mathcal{G}_t)$, during $[t - \tau, t]$. According to the definition of rate matrix, in $[t - \tau, t]$, the number of transitions from f^i to \bar{f}^i , namely J_{f^i, \bar{f}^i} , follows the Poisson distribution, i.e., $J_{f^i, \bar{f}^i} \sim \text{Poisson}(\tau \tilde{\mathbf{R}}_{\theta,t}^i(f^i, \bar{f}^i))$. For categorical data (e.g., node type), multiple transitions in $[t - \tau, t]$ are invalid and meaningless. In other words, for the i -th node, if the total number of transitions $\sum_{\bar{f}^i} J_{f^i, \bar{f}^i} > 1$, f^i keeps unchanged in $[t - \tau, t]$; otherwise, if $\sum_{\bar{f}^i} J_{f^i, \bar{f}^i} = 1$ and $J_{f^i, s} > 1$, i.e., there is exact 1 transition, from f^i to s , in $[t - \tau, t]$. The Appendix summarizes A step-by-step sampling algorithm in Algorithm 2.

Remark 3.4. The sampling error of τ -leaping is linear to C_{err} [7], where C_{err} is the approximation error of the reverse rate matrix: $\sum_{\mathcal{G} \neq \bar{\mathcal{G}}} \left| \tilde{\mathbf{R}}_t(\mathcal{G}, \bar{\mathcal{G}}) - \tilde{\mathbf{R}}_{\theta,t}(\mathcal{G}, \bar{\mathcal{G}}) \right| \leq C_{\text{err}}$. Interested readers are referred to check Theorem 1 from [7]. Our Theorem 3.3 shows the connection between our training loss and C_{err} , which further verifies the correctness of our training loss.

3.5 Model Instantiation

As mentioned in Section 3.3, the parametric backbone $p_{0|t}^\theta(\mathcal{G}_0|\mathcal{G}_t)$ is a graph-to-graph mapping whose input is the noisy graph \mathcal{G}_t and its output is the predicted denoised graph \mathcal{G}_0 . There exists a broad range of neural network architectures. Notably, DiGress [62] uses a graph Transformer as the backbone model, a decent reference for our continuous-time framework. We name our model with the graph transformer (GT) backbone model as DISCO-GT and its detailed configuration is introduced in Appendix F.3. The main advantage of the GT is its long-range interaction thanks to the complete attention graph from the self-attention mechanism; however, the architecture is very complex and includes multi-head self-attention modules, leading to expensive computation.

Beyond GTs, in this paper, we posit that a regular message-passing neural network (MPNN) [15] architecture should be a promising architecture for graph-to-graph mapping. It is recognized that the expressiveness of MPNNs might not be as good as GTs [28, 6], e.g., MPNN cannot model long-range interactions. However, in our setting, the absence of an edge is viewed as a special type of edge. In other words, the whole graph is complete; therefore, such a limitation of MPNN is naturally mitigated, which is verified by our empirical evaluations.

Concretely, an MPNN-based graph-to-graph mapping is presented as follows, and our framework with MPNN is named DISCO-MPNN. Given a graph $\mathcal{G} = (\mathbf{E}, \mathbf{F})$, where $\mathbf{E} \in \{1, \dots, a, a+1\}^{n \times n}$, $\mathbf{F} \in \{1, \dots, b\}^n$, we first transform both the matrix \mathbf{E} and \mathbf{F} into their one-hot representations $\mathbf{E}_{\text{OH}} \in \mathbb{R}^{n \times n \times (a+1)}$ and $\mathbf{F}_{\text{OH}} \in \mathbb{R}^{n \times b}$. Then, some auxiliary features (e.g., the # of connected components and the # of specific motifs) are extracted: $\mathbf{F}_{\text{aux}}, \mathbf{y}_{\text{aux}} = \text{Aux}(\mathbf{E}_{\text{OH}})$ to overcome the expressiveness limitation of MPNNs [10]. Here \mathbf{F}_{aux} and \mathbf{y}_{aux} are the node-level and global auxiliary features, respectively. Note that a similar auxiliary feature engineering is also applied in DiGress [62]. More details about the Aux can be found in Appendix E. Then, three multi-layer perceptrons (MLPs) are used to map node features $\mathbf{F}_{\text{OH}} \oplus \mathbf{F}_{\text{aux}}$, edge features \mathbf{E}_{OH} , and global features \mathbf{y}_{aux} into a common hidden space as $\mathbf{F}_{\text{hidden}} = \text{MLP}(\mathbf{F}_{\text{OH}} \oplus \mathbf{F}_{\text{aux}})$, $\mathbf{E}_{\text{hidden}} = \text{MLP}(\mathbf{E}_{\text{OH}})$, $\mathbf{y}_{\text{hidden}} = \text{MLP}(\mathbf{y}_{\text{aux}})$, where \oplus is a concatenation operator. The following formulas present the update of node representations (e.g., $\mathbf{r}^i = \mathbf{F}(i, :)$), edge representations (e.g., $\mathbf{r}^{(i,j)} = \mathbf{E}(i, j, :)$), and global representation \mathbf{y} in an MPNN layer, where we omit the subscript hidden if it does not cause ambiguity.

$$\mathbf{r}^i \leftarrow \text{FiLM} \left(\text{FiLM} \left(\mathbf{r}^i, \text{MLP} \left(\frac{\sum_{j=1}^n \mathbf{r}^{(j,i)}}{n} \right) \right), \mathbf{y} \right), \quad (10)$$

$$\mathbf{r}^{(i,j)} \leftarrow \text{FiLM}(\text{FiLM}(\mathbf{r}^{(i,j)}, \mathbf{r}^i \odot \mathbf{r}^j), \mathbf{y}), \quad (11)$$

$$\mathbf{y} \leftarrow \mathbf{y} + \text{PNA}(\{\mathbf{r}^i\}_{i=1}^n) + \text{PNA}(\{\mathbf{r}^{(i,j)}\}_{i,j=1}^n), \quad (12)$$

where the edge embeddings are aggregated by mean pooling (i.e., $\frac{\sum_{j=1}^n \mathbf{r}^{(j,i)}}{n}$); the node pair embeddings are passed to edges by Hadamard product (i.e., $\mathbf{r}^i \odot \mathbf{r}^j$); edge/node embeddings are merged to the global embedding \mathbf{y} via the PNA module [11]; Some FiLM modules [49] are used for the interaction between node/edge/global embeddings. More details about the PNA and FiLM are in Appendix E. In this paper, we name Eqs. (10), (11), and (12) on all nodes/edges together as an MPNN layer, $\mathbf{F}, \mathbf{E}, \mathbf{y} \leftarrow \text{MPNN}(\mathbf{F}, \mathbf{E}, \mathbf{y})$. Stacking multiple MPNN layers can improve the capacity of the graph-to-graph backbone. In the final layer, two readout MLPs are used to project the node/edge embeddings into their input dimensions, $\text{MLP}(\mathbf{F}) \in \mathbb{R}^{n \times b}$ and $\text{MLP}(\mathbf{E}) \in \mathbb{R}^{n \times n \times (a+1)}$. These two sets of logits are output after wrapped with softmax.

Note that both the proposed MPNN layer and the GT layer from DiGress [62] use the PNA and FiLM to merge node/edge/global embeddings, but MPNN does not have a multi-head self-attention layer so that the computation overhead is lower.

3.6 Permutation Equivariance and Invariance

Reordering the nodes keeps the property of a given graph, which is known as permutation invariance. In addition, for a given function if its input is permuted and its output is permuted accordingly, such a behavior is known as permutation equivariance. In this subsection, we analyze permutation-equivariance/invariance of the (1) diffusion framework (Lemmas 3.5, 3.6, and 3.7), (2) sampling density (Theorem 3.8), and (3) training loss (Theorem 3.9).

Lemma 3.5 (permutation-equivariant layer). *The proposed MPNN layer (Eqs. (10), (11), and (12)) is permutation-equivariant.*

The auxiliary features from the Aux are also permutation-equivariant (see Appendix E). Thus, the whole MPNN-based graph-to-graph backbone $p_{0|t}^\theta$ is permutation-equivariant. Note that the GT-based backbone model from DiGress [62] is also permutation-equivariant whose proof is omitted as it is not our main contribution. Next, we show the permutation invariance of the forward and reverse rate matrices of DISCO.

Lemma 3.6 (Permutation-invariant rate matrices). *The forward rate matrix of DISCO is permutation-invariant if it is factorized as Eq. (5). The parametric reverse rate matrix of DISCO (Eq. (7)) is permutation-invariant whenever the graph-to-graph backbone $p_{0|t}^\theta$ is permutation-equivariant.*

Lemma 3.7 (Permutation-invariant transition probability). *For CTMC satisfying the Kolmogorov forward equation (Eq. (1)), if the rate matrix is permutation-invariant (i.e., $\mathbf{R}_t(\mathbf{x}_i, \mathbf{x}_j) = \mathbf{R}_t(\mathcal{P}(\mathbf{x}_i), \mathcal{P}(\mathbf{x}_j))$), the transition probability is permutation-invariant (i.e., $q_{t|s}(\mathbf{x}_t | \mathbf{x}_s) = q_{t|s}(\mathcal{P}(\mathbf{x}_t) | \mathcal{P}(\mathbf{x}_s))$), where \mathcal{P} is a permutation.*

Based on Lemmas 3.6 and 3.7, DISCO’s parametric reverse transition probability is permutation-invariant. The next theorem shows the permutation-invariance of the sampling probability.

Theorem 3.8 (Permutation-invariant sampling probability). *If both the reference distribution π_{ref} and the reverse transition probability are permutation-invariant, the parametric sampling distribution $p_0^\theta(\mathcal{G}_0)$ is permutation-invariant.*

In addition, the next theorem shows the permutation invariance of the training loss.

Theorem 3.9 (Permutation-invariant training loss). *The proposed training objective Eq. (9) is invariant to any permutation of the input graph \mathcal{G}_0 if the graph-to-graph backbone $p_{0|t}^\theta$ is permutation-equivariant.*

4 Experiments

This section presents the effectiveness evaluation on the plain graph (Section 4.1) and molecule graphs (Section 4.2), an efficiency study (Section 4.3), and an ablation study (Section 4.4). Detailed experimental settings (Sections F.1-F.3), additional effectiveness evaluation (Section F.4), convergence study (Section F.5), and visualization of the generated graphs and the diffusion process (Section F.6) are in Appendix.

4.1 Plain Graph Generation

Datasets and metrics. Datasets SBM, Planar [43], and Community [68] are used. The relative squared Maximum Mean Discrepancy (MMD) for degree distributions (Deg.), clustering coefficient distributions (Clus.), and orbit counts (Orb.) distributions (the number of occurrences of substructures with 4 nodes), Uniqueness(%), Novelty(%), and Validity(%) are chosen as metrics. Results on Community [68] are reported in Table 8 in Appendix. Appendix F.2.2 provides more details about the datasets and metrics.

Baseline methods. GraphRNN [68], GRAN [35], GG-GAN [30], MolGAN [8], SPECTRE [43], ConGress [62], DiGress [62] are chosen.

Results and analysis. Table 1 shows

- DISCO-GT can obtain competitive performance against the SOTA, DiGress, which is reasonable because both models share the same graph-to-graph backbone, graph Transformer. Note that DiGress’s performance in terms of Validity is not the statistics reported in the paper but from their latest model checkpoint³. In fact, we found it very hard for DiGress and DISCO-GT to learn to generate valid SBM/Planar graphs. These two datasets have only 200 graphs, but sometimes only after $> 10,000$ epochs training, the Validity percentage can be $> 50\%$. Additionally, DISCO-GT provides extra flexibility during sampling by adjusting the τ . This is important: our models can still trade-off between the sampling efficiency and quality even after the model is trained and fixed.
- In general, DISCO-MPNN has competitive performance against DISCO-GT in terms of Deg., Clus., and Orb. However, its performance is worse compared to DISCO-GT in terms of Validity, which might be related to the difference in model expressiveness. Studying the graph-to-graph model expressiveness would be an interesting future direction, e.g., generating valid SBM and Planar graphs. As far as we know, no work exists in this direction.

4.2 Molecule Graph Generation

Dataset and metrics. The datasets QM9 [52], MOSES [50], and GuacaMol [5] are chosen. For QM9, Uniqueness, Novelty, and Validity are reported in Table 2. For MOSES, metrics including Uniqueness, Novelty, Validity, Filter, FCD, SNN, and Scaf are reported in Table 3. For GuacaMol, metrics including Valid, Unique, Novel, KL div, and FCD are reported in Table 4. More details about the datasets and the metrics are in Appendix F.2.3.

³<https://github.com/cvignac/DiGress/blob/main/README.md>

Table 1: Generation performance on SBM and Planar datasets.

Model	Deg.↓	Clus.↓	Orb.↓	Unique ↑	Novel ↑	Valid ↑
<i>SBM dataset</i>						
GraphRNN [68]	6.9	1.7	3.1	100.0	100.0	5.0
GRAN [35]	14.1	1.7	2.1	100.0	100.0	25.0
GG-GAN [30]	4.4	2.1	2.3	100.0	100.0	0.0
MolGAN [8]	29.4	3.5	2.8	95.0	100.0	10.0
SPECTRE [43]	1.9	1.6	1.6	100.0	100.0	52.5
ConGress [62]	34.1	3.1	4.5	0.0	0.0	0.0
DiGress [62]	1.6	1.5	1.7	100.0	100.0	67.5
DISCO-MPNN	1.8±0.2	0.8±0.1	2.7±0.4	100.0±0.0	100.0±0.0	41.9±2.2
DISCO-GT	0.8±0.2	0.8±0.4	2.0±0.5	100.0±0.0	100.0±0.0	66.2±1.4
<i>Planar dataset</i>						
GraphRNN [68]	24.5	9.0	2508.0	100.0	100.0	0.0
GRAN [35]	3.5	1.4	1.8	85.0	2.5	97.5
GG-GAN [30]	315.0	8.3	2062.6	100.0	100.0	0.0
MolGAN [8]	4.5	10.2	2346.0	25.0	100.0	0.0
SPECTRE [43]	2.5	2.5	2.4	100.0	100.0	25.0
ConGress [62]	23.8	8.8	2590.0	0.0	0.0	0.0
DiGress [62]	1.4	1.2	1.7	100.0	100.0	85.0
DISCO-MPNN	1.4±0.3	1.4±0.4	6.4±1.6	100.0±0.0	100.0±0.0	33.8±2.7
DISCO-GT	1.2±0.5	1.3±0.5	1.7±0.7	100.0±0.0	100.0±0.0	83.6±2.1

Table 2: Generation performance (%) on QM9 dataset. V., U., and N. mean Valid, Unique, and Novel.

Model	Valid ↑	V.U. ↑	V.U.N. ↑
CharacterVAE [16]	10.3	7.0	6.3
GrammarVAE[31]	60.2	5.6	4.5
GraphVAE [56]	55.7	42.0	26.1
GT-VAE [47]	74.6	16.8	15.8
Set2GraphVAE [61]	59.9	56.2	-
GG-GAN [30]	51.2	24.4	24.4
MolGAN [8]	98.1	10.2	9.6
SPECTRE [43]	87.3	31.2	29.1
GraphNVP [42]	83.1	82.4	-
GDSS [27]	95.7	94.3	-
ConGress [62]	98.9	95.7	38.3
DiGress [62]	99.0	95.2	31.8
GRAPHARM [29]	90.3	86.3	-
DISCO-GT	99.3±0.6	98.9±0.6	56.2±0.4
DISCO-MPNN	98.9±0.7	98.7±0.5	68.7±0.2

Baseline methods. CharacterVAE [16], GrammarVAE [31], GraphVAE [56], GT-VAE [47], Set2GraphVAE [61], GG-GAN [30], MolGAN [8], SPECTRE [43], GraphNVP [42], GDSS [27], ConGress [62], DiGress [62], GRAPHARM [29], VAE [17], JT-VAE [24], GraphINVENT [45], LSTM [54], NAGVAE [33], and MCTS [23] are chosen.

Results and analysis. Table 2 shows the performance on QM9 dataset. Our observation is consistent with the performance comparison on plain datasets: (1) DISCO-GT obtains slightly better or at least competitive performance against DiGress due to the shared graph-to-graph backbone, but our framework offers extra flexibility in the sampling process; (2) DISCO-MPNN obtains decent performance in terms of Validity, Uniqueness, and Novelty comparing with DISCO-GT.

Tables 3 and 4 show the performance on MOSES and GuacaMol datasets which further verifies that the proposed DISCO’s performance is on par with the SOTA general graph generative models, DiGress.

Table 3: Generation performance on MOSES. VAE, JT-VAE, and GraphINVENT have hard-coded rules to ensure high validity.

Model	Valid \uparrow	Unique \uparrow	Novel \uparrow	Filters \uparrow	FCD \downarrow	SNN \uparrow	Scaf \uparrow
VAE [17]	97.7	98.8	69.5	99.7	0.57	0.58	5.9
JT-VAE [24]	100.0	100.0	99.9	97.8	1.00	0.53	10.0
GraphINVENT [45]	96.4	99.8	N/A	95.0	1.22	0.54	12.7
ConGress [62]	83.4	99.9	96.4	94.8	1.48	0.50	16.4
DiGress [62]	85.7	100.0	95.0	97.1	1.19	0.52	14.8
DISCO-GT	88.3	100.0	97.7	95.6	1.44	0.50	15.1
DISCO-MPNN	83.9	100.0	98.8	87.3	1.63	0.48	13.5

Table 4: Generation performance on GuacaMol. LSTM, NAGVAE, and MCTS are tailored for molecule datasets; ConGress, DiGress, and DISCO are general graph generation models.

Model	Valid \uparrow	Unique \uparrow	Novel \uparrow	KL div \uparrow	FCD \uparrow
LSTM [54]	95.9	100.0	91.2	99.1	91.3
NAGVAE [33]	92.9	95.5	100.0	38.4	0.9
MCTS [23]	100.0	100.0	95.4	82.2	1.5
ConGress [62]	0.1	100.0	100.0	36.1	0.0
DiGress [62]	85.2	100.0	99.9	92.9	68.0
DISCO-GT	86.6	100.0	99.9	92.6	59.7
DISCO-MPNN	68.7	100.0	96.4	77.0	36.4

Table 5: Efficiency comparison of backbone models on community dataset. Inference and Backpropagation are the time (second/iteration) for model inference and backpropagation training.

	GT	MPNN
# of Parameters	14,216,707	7,047,427
Inference	0.065	0.022
Backpropagation	0.034	0.018

4.3 Efficiency Study

A major computation bottleneck is the graph-to-graph backbone $p_{0|t}^\theta$, which is based on graph transformer (GT) or message-passing neural networks (MPNN). We compare the number of parameters, the inference time, and the back-propagation time of GT and MPNN in Table 5. For a fair comparison, we set all the hidden dimensions of GT and MPNN as 256 and the number of layers of both models as 5. We use the Community [68] dataset and set the batch size as 64. Table 5 shows that GT has a larger model capacity and more parameters at the expense of more expensive model training and inference.

4.4 Ablation Study

An ablation study on DISCO with different backbones (GT vs. MPNN), reference distributions (marginal vs. uniform), and the number of sampling steps (1, 5, 10, 30, 100, and 500) is presented in Table 6. The number of sampling steps is determined by τ , which is $\text{round}(\frac{1}{\tau})$ if the converged time is set as $T = 1$. Overall, we observe the following results.

- GT overall performs better than MPNN as the backbone model in terms of effectiveness.
- Generally, the fewer sampling steps, the lower the generation quality. In some cases (e.g., the marginal reference distribution) with the sampling steps varying significantly (e.g., from 500 to 30), the performance change is still very slight, implying our method’s high robustness in sampling steps.
- The marginal reference distribution is better than the uniform distribution, consistent with the conclusion from DiGress [62].

Table 6: Ablation study (%) on QM9 dataset. V., U., and N. mean Valid, Unique, and Novel.

Backbone	Ref. Dist.	Sampling steps	Valid \uparrow	V.U. \uparrow	V.U.N. \uparrow
GT	Marginal	500	99.3 \pm 0.6	98.9 \pm 0.6	56.2 \pm 0.4
		100	98.7 \pm 0.5	98.5 \pm 0.4	58.8 \pm 0.4
		30	97.9 \pm 1.2	97.6 \pm 1.1	59.2 \pm 0.8
		10	95.3 \pm 1.9	94.8 \pm 1.6	62.1 \pm 0.9
		5	93.0 \pm 1.7	92.4 \pm 1.3	64.9 \pm 1.1
		1	76.1 \pm 2.3	73.9 \pm 1.6	62.9 \pm 1.8
	Uniform	500	94.1 \pm 0.9	92.9 \pm 0.5	56.6 \pm 0.4
		100	91.5 \pm 1.0	90.3 \pm 0.9	54.4 \pm 1.2
		30	88.7 \pm 1.6	86.9 \pm 1.0	58.6 \pm 2.1
		10	84.5 \pm 2.3	80.4 \pm 1.7	59.8 \pm 1.8
		5	77.0 \pm 2.5	69.9 \pm 1.5	56.1 \pm 3.5
		1	44.9 \pm 3.1	35.1 \pm 3.4	29.6 \pm 2.5
MPNN	Marginal	500	98.9 \pm 0.7	98.7 \pm 0.5	68.7 \pm 0.2
		100	98.4 \pm 1.1	98.0 \pm 1.0	69.1 \pm 0.6
		30	97.7 \pm 1.2	97.5 \pm 0.8	70.4 \pm 1.1
		10	92.3 \pm 1.9	91.9 \pm 2.2	66.4 \pm 1.7
		5	88.8 \pm 3.3	87.1 \pm 2.8	67.3 \pm 2.9
		1	64.4 \pm 2.7	63.2 \pm 1.9	55.8 \pm 1.4
	Uniform	500	93.5 \pm 1.7	93.2 \pm 1.1	64.9 \pm 1.0
		100	93.1 \pm 2.1	92.6 \pm 1.7	66.2 \pm 1.9
		30	87.1 \pm 1.8	86.8 \pm 1.1	64.0 \pm 1.0
		10	83.7 \pm 3.2	81.9 \pm 2.1	61.3 \pm 2.0
		5	81.5 \pm 2.9	75.4 \pm 3.4	64.6 \pm 2.3
		1	71.3 \pm 2.3	42.2 \pm 4.0	36.9 \pm 3.2

5 Related Work

We present a brief literature review on diffusion generative models and their applications for graph generation tasks.

Diffusion models are a family of popular generative models [66]. Their core idea is progressively adding noise into the data and designing a parametric model to sample clean data from tractable noise reversely. Its formulation can be either interpreted from the score-matching [58, 59] or the variational autoencoder perspective [18]. Beyond the continuous-state space where the diffusion process corrupts the given data into Gaussian noise [57], some efforts propose to design the diffusion process in the discrete-state space [19]. For example, D3PM [2] designs the discrete diffusion process by cumulative product of a fixed transition probability matrix; τ -LDR [7] generalizes D3PM by formulating the diffusion process as a continuous-time Markov chain.

Diffusion generative models attract broad attention for graph generation tasks [37], for their promising applications such as molecule design [55, 20, 22, 36]. Pioneering works such as EDP-GNN [48] and GDSS [27] diffuse graph data in a continuous state space [21]. DiGress [62] is the first one-shot diffusion model to formulate graph data in discrete state space, followed by a very recent work MCD [39], both in the discrete-time setting. DruM [26] proposes to mix the diffusion process by conditioning on the endpoint in the data distribution. Edge [9] designs the diffusion process by diffusing graphs into empty graphs. Interestingly, GRAPHARM [29] uses an autoregressive diffusion model for graph generation. Besides, Liu et al. [38] apply the diffusion models for molecule property prediction. In addition to these works, there are many other task-tailored graph diffusion generative models [40, 25, 34, 51, 65, 64, 3, 63]. Interested readers are referred to this survey [37].

6 Conclusion

This paper introduces the first discrete-state continuous-time graph diffusion generative model, DISCO. Our model effectively marries continuous-time Markov Chain formulation with the discrete nature of graph data, addressing the fundamental sampling limitation of prior models. DISCO’s training objective is concise with a solid theoretical foundation. We also propose a simplified message-passing architecture to serve as the graph-to-graph backbone, which theoretically has desirable properties against permutation of node ordering and empirically demonstrates competitive performance against existing graph generative models in tests on various datasets.

7 Broader Impact

This paper presents work whose goal is to advance the field of Machine Learning. There are many potential societal consequences of our work, none of which we feel must be specifically highlighted here.

References

- [1] David F Anderson. A modified next reaction method for simulating chemical systems with time dependent propensities and delays. *The Journal of chemical physics*, 127(21), 2007.
- [2] Jacob Austin, Daniel D. Johnson, Jonathan Ho, Daniel Tarlow, and Rianne van den Berg. Structured denoising diffusion models in discrete state-spaces. In Marc’Aurelio Ranzato, Alina Beygelzimer, Yann N. Dauphin, Percy Liang, and Jennifer Wortman Vaughan, editors, *Advances in Neural Information Processing Systems 34: Annual Conference on Neural Information Processing Systems 2021, NeurIPS 2021, December 6-14, 2021, virtual*, pages 17981–17993, 2021.
- [3] Fan Bao, Min Zhao, Zhongkai Hao, Peiyao Li, Chongxuan Li, and Jun Zhu. Equivariant energy-guided sde for inverse molecular design. In *The eleventh international conference on learning representations*, 2023.
- [4] D Brook. On the distinction between the conditional probability and the joint probability approaches in the specification of nearest-neighbour systems. *Biometrika*, 51(3/4):481–483, 1964.
- [5] Nathan Brown, Marco Fiscato, Marwin H. S. Segler, and Alain C. Vaucher. Guacamol: Benchmarking models for de novo molecular design. *J. Chem. Inf. Model.*, 59(3):1096–1108, 2019.
- [6] Chen Cai, Truong Son Hy, Rose Yu, and Yusu Wang. On the connection between MPNN and graph transformer. In Andreas Krause, Emma Brunskill, Kyunghyun Cho, Barbara Engelhardt, Sivan Sabato, and Jonathan Scarlett, editors, *International Conference on Machine Learning, ICML 2023, 23-29 July 2023, Honolulu, Hawaii, USA*, volume 202 of *Proceedings of Machine Learning Research*, pages 3408–3430. PMLR, 2023.
- [7] Andrew Campbell, Joe Benton, Valentin De Bortoli, Thomas Rainforth, George Deligiannidis, and Arnaud Doucet. A continuous time framework for discrete denoising models. In *NeurIPS*, 2022.
- [8] Nicola De Cao and Thomas Kipf. Molgan: An implicit generative model for small molecular graphs. *CoRR*, abs/1805.11973, 2018.
- [9] Xiaohui Chen, Jiaying He, Xu Han, and Li-Ping Liu. Efficient and degree-guided graph generation via discrete diffusion modeling. In *Proceedings of the 40th International Conference on Machine Learning*, pages 4585–4610, 2023.
- [10] Zhengdao Chen, Lei Chen, Soledad Villar, and Joan Bruna. Can graph neural networks count substructures? In Hugo Larochelle, Marc’Aurelio Ranzato, Raia Hadsell, Maria-Florina Balcan, and Hsuan-Tien Lin, editors, *Advances in Neural Information Processing Systems 33: Annual Conference on Neural Information Processing Systems 2020, NeurIPS 2020, December 6-12, 2020, virtual*, 2020.
- [11] Gabriele Corso, Luca Cavalleri, Dominique Beaini, Pietro Liò, and Petar Velickovic. Principal neighbourhood aggregation for graph nets. In Hugo Larochelle, Marc’Aurelio Ranzato, Raia

- Hadsell, Maria-Florina Balcan, and Hsuan-Tien Lin, editors, *Advances in Neural Information Processing Systems 33: Annual Conference on Neural Information Processing Systems 2020, NeurIPS 2020, December 6-12, 2020, virtual*, 2020.
- [12] Daniel T Gillespie. A general method for numerically simulating the stochastic time evolution of coupled chemical reactions. *Journal of computational physics*, 22(4):403–434, 1976.
- [13] Daniel T Gillespie. Exact stochastic simulation of coupled chemical reactions. *The journal of physical chemistry*, 81(25):2340–2361, 1977.
- [14] Daniel T Gillespie. Approximate accelerated stochastic simulation of chemically reacting systems. *The Journal of chemical physics*, 115(4):1716–1733, 2001.
- [15] Justin Gilmer, Samuel S. Schoenholz, Patrick F. Riley, Oriol Vinyals, and George E. Dahl. Neural message passing for quantum chemistry. In Doina Precup and Yee Whye Teh, editors, *Proceedings of the 34th International Conference on Machine Learning, ICML 2017, Sydney, NSW, Australia, 6-11 August 2017*, volume 70 of *Proceedings of Machine Learning Research*, pages 1263–1272. PMLR, 2017.
- [16] Rafael Gómez-Bombarelli, David Duvenaud, José Miguel Hernández-Lobato, Jorge Aguilera-Iparraguirre, Timothy D. Hirzel, Ryan P. Adams, and Alán Aspuru-Guzik. Automatic chemical design using a data-driven continuous representation of molecules. *CoRR*, abs/1610.02415, 2016.
- [17] Rafael Gómez-Bombarelli, Jennifer N Wei, David Duvenaud, José Miguel Hernández-Lobato, Benjamín Sánchez-Lengeling, Dennis Sheberla, Jorge Aguilera-Iparraguirre, Timothy D Hirzel, Ryan P Adams, and Alán Aspuru-Guzik. Automatic chemical design using a data-driven continuous representation of molecules. *ACS central science*, 4(2):268–276, 2018.
- [18] Jonathan Ho, Ajay Jain, and Pieter Abbeel. Denoising diffusion probabilistic models. In Hugo Larochelle, Marc’Aurelio Ranzato, Raia Hadsell, Maria-Florina Balcan, and Hsuan-Tien Lin, editors, *Advances in Neural Information Processing Systems 33: Annual Conference on Neural Information Processing Systems 2020, NeurIPS 2020, December 6-12, 2020, virtual*, 2020.
- [19] Emiel Hoogeboom, Didrik Nielsen, Priyank Jaini, Patrick Forré, and Max Welling. Argmax flows and multinomial diffusion: Learning categorical distributions. In Marc’Aurelio Ranzato, Alina Beygelzimer, Yann N. Dauphin, Percy Liang, and Jennifer Wortman Vaughan, editors, *Advances in Neural Information Processing Systems 34: Annual Conference on Neural Information Processing Systems 2021, NeurIPS 2021, December 6-14, 2021, virtual*, pages 12454–12465, 2021.
- [20] Emiel Hoogeboom, Victor Garcia Satorras, Clément Vignac, and Max Welling. Equivariant diffusion for molecule generation in 3d. In Kamalika Chaudhuri, Stefanie Jegelka, Le Song, Csaba Szepesvári, Gang Niu, and Sivan Sabato, editors, *International Conference on Machine Learning, ICML 2022, 17-23 July 2022, Baltimore, Maryland, USA*, volume 162 of *Proceedings of Machine Learning Research*, pages 8867–8887. PMLR, 2022.
- [21] Han Huang, Leilei Sun, Bowen Du, Yanjie Fu, and Weifeng Lv. Graphgdp: Generative diffusion processes for permutation invariant graph generation. In Xingquan Zhu, Sanjay Ranka, My T. Thai, Takashi Washio, and Xindong Wu, editors, *IEEE International Conference on Data Mining, ICDM 2022, Orlando, FL, USA, November 28 - Dec. 1, 2022*, pages 201–210. IEEE, 2022.
- [22] Lei Huang, Hengtong Zhang, Tingyang Xu, and Ka-Chun Wong. MDM: molecular diffusion model for 3d molecule generation. In Brian Williams, Yiling Chen, and Jennifer Neville, editors, *Thirty-Seventh AAAI Conference on Artificial Intelligence, AAAI 2023, Thirty-Fifth Conference on Innovative Applications of Artificial Intelligence, IAAI 2023, Thirteenth Symposium on Educational Advances in Artificial Intelligence, EAAI 2023, Washington, DC, USA, February 7-14, 2023*, pages 5105–5112. AAAI Press, 2023.
- [23] Jan H Jensen. A graph-based genetic algorithm and generative model/monte carlo tree search for the exploration of chemical space. *Chemical science*, 10(12):3567–3572, 2019.
- [24] Wengong Jin, Regina Barzilay, and Tommi S. Jaakkola. Junction tree variational autoencoder for molecular graph generation. In Jennifer G. Dy and Andreas Krause, editors, *Proceedings of the 35th International Conference on Machine Learning, ICML 2018, Stockholmsmässan, Stockholm, Sweden, July 10-15, 2018*, volume 80 of *Proceedings of Machine Learning Research*, pages 2328–2337. PMLR, 2018.

- [25] Bowen Jing, Gabriele Corso, Jeffrey Chang, Regina Barzilay, and Tommi S. Jaakkola. Torsional diffusion for molecular conformer generation. In Sanmi Koyejo, S. Mohamed, A. Agarwal, Danielle Belgrave, K. Cho, and A. Oh, editors, *Advances in Neural Information Processing Systems 35: Annual Conference on Neural Information Processing Systems 2022, NeurIPS 2022, New Orleans, LA, USA, November 28 - December 9, 2022*, 2022.
- [26] Jaehyeong Jo, Dongki Kim, and Sung Ju Hwang. Graph generation with destination-predicting diffusion mixture. *OpenReview*, 2023.
- [27] Jaehyeong Jo, Seul Lee, and Sung Ju Hwang. Score-based generative modeling of graphs via the system of stochastic differential equations. In Kamalika Chaudhuri, Stefanie Jegelka, Le Song, Csaba Szepesvári, Gang Niu, and Sivan Sabato, editors, *International Conference on Machine Learning, ICML 2022, 17-23 July 2022, Baltimore, Maryland, USA*, volume 162 of *Proceedings of Machine Learning Research*, pages 10362–10383. PMLR, 2022.
- [28] Jinwoo Kim, Dat Nguyen, Seonwoo Min, Sungjun Cho, Moontae Lee, Honglak Lee, and Seunghoon Hong. Pure transformers are powerful graph learners. In Sanmi Koyejo, S. Mohamed, A. Agarwal, Danielle Belgrave, K. Cho, and A. Oh, editors, *Advances in Neural Information Processing Systems 35: Annual Conference on Neural Information Processing Systems 2022, NeurIPS 2022, New Orleans, LA, USA, November 28 - December 9, 2022*, 2022.
- [29] Lingkai Kong, Jiaming Cui, Haotian Sun, Yuchen Zhuang, B. Aditya Prakash, and Chao Zhang. Autoregressive diffusion model for graph generation. In Andreas Krause, Emma Brunskill, Kyunghyun Cho, Barbara Engelhardt, Sivan Sabato, and Jonathan Scarlett, editors, *International Conference on Machine Learning, ICML 2023, 23-29 July 2023, Honolulu, Hawaii, USA*, volume 202 of *Proceedings of Machine Learning Research*, pages 17391–17408. PMLR, 2023.
- [30] Igor Krawczuk, Pedro Abranches, Andreas Loukas, and Volkan Cevher. Gg-gan: A geometric graph generative adversarial network, 2021. In URL <https://openreview.net/forum>, 2020.
- [31] Matt J. Kusner and José Miguel Hernández-Lobato. GANS for sequences of discrete elements with the gumbel-softmax distribution. *CoRR*, abs/1611.04051, 2016.
- [32] Youngchun Kwon, Dongseon Lee, Youn-Suk Choi, Kyoham Shin, and Seokho Kang. Compressed graph representation for scalable molecular graph generation. *J. Cheminformatics*, 12(1):58, 2020.
- [33] Youngchun Kwon, Dongseon Lee, Youn-Suk Choi, Kyoham Shin, and Seokho Kang. Compressed graph representation for scalable molecular graph generation. *Journal of Cheminformatics*, 12:1–8, 2020.
- [34] Seul Lee, Jaehyeong Jo, and Sung Ju Hwang. Exploring chemical space with score-based out-of-distribution generation. In Andreas Krause, Emma Brunskill, Kyunghyun Cho, Barbara Engelhardt, Sivan Sabato, and Jonathan Scarlett, editors, *International Conference on Machine Learning, ICML 2023, 23-29 July 2023, Honolulu, Hawaii, USA*, volume 202 of *Proceedings of Machine Learning Research*, pages 18872–18892. PMLR, 2023.
- [35] Renjie Liao, Yujia Li, Yang Song, Shenlong Wang, William L. Hamilton, David Duvenaud, Raquel Urtasun, and Richard S. Zemel. Efficient graph generation with graph recurrent attention networks. In Hanna M. Wallach, Hugo Larochelle, Alina Beygelzimer, Florence d’Alché-Buc, Emily B. Fox, and Roman Garnett, editors, *Advances in Neural Information Processing Systems 32: Annual Conference on Neural Information Processing Systems 2019, NeurIPS 2019, December 8-14, 2019, Vancouver, BC, Canada*, pages 4257–4267, 2019.
- [36] Haitao Lin, Yufei Huang, Meng Liu, Xuanjing Li, Shuiwang Ji, and Stan Z. Li. Diffbp: Generative diffusion of 3d molecules for target protein binding. *CoRR*, abs/2211.11214, 2022.
- [37] Chengyi Liu, Wenqi Fan, Yunqing Liu, Jiatong Li, Hang Li, Hui Liu, Jiliang Tang, and Qing Li. Generative diffusion models on graphs: Methods and applications. In *Proceedings of the Thirty-Second International Joint Conference on Artificial Intelligence, IJCAI 2023, 19th-25th August 2023, Macao, SAR, China*, pages 6702–6711. ijcai.org, 2023.
- [38] Gang Liu, Eric Inae, Tong Zhao, Jiabin Xu, Tengfei Luo, and Meng Jiang. Data-centric learning from unlabeled graphs with diffusion model. *Advances in neural information processing systems*, 36, 2023.
- [39] Gang Liu, Jiabin Xu, Tengfei Luo, and Meng Jiang. Inverse molecular design with multi-conditional diffusion guidance. *arXiv preprint arXiv:2401.13858*, 2024.

- [40] Shitong Luo, Chence Shi, Minkai Xu, and Jian Tang. Predicting molecular conformation via dynamic graph score matching. In Marc’Aurelio Ranzato, Alina Beygelzimer, Yann N. Dauphin, Percy Liang, and Jennifer Wortman Vaughan, editors, *Advances in Neural Information Processing Systems 34: Annual Conference on Neural Information Processing Systems 2021, NeurIPS 2021, December 6-14, 2021, virtual*, pages 19784–19795, 2021.
- [41] Siwei Lyu. Interpretation and generalization of score matching. In Jeff A. Bilmes and Andrew Y. Ng, editors, *UAI 2009, Proceedings of the Twenty-Fifth Conference on Uncertainty in Artificial Intelligence, Montreal, QC, Canada, June 18-21, 2009*, pages 359–366. AUAI Press, 2009.
- [42] Kaushalya Madhawa, Katushiko Ishiguro, Kosuke Nakago, and Motoki Abe. Graphnvp: An invertible flow model for generating molecular graphs. *CoRR*, abs/1905.11600, 2019.
- [43] Karolis Martinkus, Andreas Loukas, Nathanaël Perraudin, and Roger Wattenhofer. SPECTRE: spectral conditioning helps to overcome the expressivity limits of one-shot graph generators. In Kamalika Chaudhuri, Stefanie Jegelka, Le Song, Csaba Szepesvári, Gang Niu, and Sivan Sabato, editors, *International Conference on Machine Learning, ICML 2022, 17-23 July 2022, Baltimore, Maryland, USA*, volume 162 of *Proceedings of Machine Learning Research*, pages 15159–15179. PMLR, 2022.
- [44] Rocío Mercado, Tobias Rastemo, Edvard Lindelöf, Günter Klambauer, Ola Engkvist, Hongming Chen, and Esben Jannik Bjerrum. Graph networks for molecular design. *Mach. Learn. Sci. Technol.*, 2(2):25023, 2021.
- [45] Rocío Mercado, Tobias Rastemo, Edvard Lindelöf, Günter Klambauer, Ola Engkvist, Hongming Chen, and Esben Jannik Bjerrum. Graph networks for molecular design. *Machine Learning: Science and Technology*, 2(2):025023, 2021.
- [46] Erxue Min, Runfa Chen, Yatao Bian, Tingyang Xu, Kangfei Zhao, Wenbing Huang, Peilin Zhao, Junzhou Huang, Sophia Ananiadou, and Yu Rong. Transformer for graphs: An overview from architecture perspective. *CoRR*, abs/2202.08455, 2022.
- [47] Joshua Mitton, Hans M. Senn, Klaas Wynne, and Roderick Murray-Smith. A graph VAE and graph transformer approach to generating molecular graphs. *CoRR*, abs/2104.04345, 2021.
- [48] Chenhao Niu, Yang Song, Jiaming Song, Shengjia Zhao, Aditya Grover, and Stefano Ermon. Permutation invariant graph generation via score-based generative modeling. In Silvia Chiappa and Roberto Calandra, editors, *The 23rd International Conference on Artificial Intelligence and Statistics, AISTATS 2020, 26-28 August 2020, Online [Palermo, Sicily, Italy]*, volume 108 of *Proceedings of Machine Learning Research*, pages 4474–4484. PMLR, 2020.
- [49] Ethan Perez, Florian Strub, Harm de Vries, Vincent Dumoulin, and Aaron C. Courville. Film: Visual reasoning with a general conditioning layer. In Sheila A. McIlraith and Kilian Q. Weinberger, editors, *Proceedings of the Thirty-Second AAAI Conference on Artificial Intelligence, (AAAI-18), the 30th innovative Applications of Artificial Intelligence (IAAI-18), and the 8th AAAI Symposium on Educational Advances in Artificial Intelligence (EAAI-18), New Orleans, Louisiana, USA, February 2-7, 2018*, pages 3942–3951. AAAI Press, 2018.
- [50] Daniil Polykovskiy, Alexander Zhebrak, Benjamín Sánchez-Lengeling, Sergey Golovanov, Oktai Tatanov, Stanislav Belyaev, Rauf Kurbanov, Aleksey Artamonov, Vladimir Aladinskiy, Mark Veselov, Artur Kadurin, Sergey I. Nikolenko, Alán Aspuru-Guzik, and Alex Zhavoronkov. Molecular sets (MOSES): A benchmarking platform for molecular generation models. *CoRR*, abs/1811.12823, 2018.
- [51] Zhuoran Qiao, Weili Nie, Arash Vahdat, Thomas F. Miller III, and Anima Anandkumar. Dynamic-backbone protein-ligand structure prediction with multiscale generative diffusion models. *CoRR*, abs/2209.15171, 2022.
- [52] Raghunathan Ramakrishnan, Pavlo O Dral, Matthias Rupp, and O Anatole Von Lilienfeld. Quantum chemistry structures and properties of 134 kilo molecules. *Scientific data*, 1(1):1–7, 2014.
- [53] Sidney I Resnick. *Adventures in stochastic processes*. Springer Science & Business Media, 1992.
- [54] Marwin HS Segler, Thierry Kogej, Christian Tyrchan, and Mark P Waller. Generating focused molecule libraries for drug discovery with recurrent neural networks. *ACS central science*, 4(1):120–131, 2018.

- [55] Chence Shi, Shitong Luo, Minkai Xu, and Jian Tang. Learning gradient fields for molecular conformation generation. In Marina Meila and Tong Zhang, editors, *Proceedings of the 38th International Conference on Machine Learning, ICML 2021, 18-24 July 2021, Virtual Event*, volume 139 of *Proceedings of Machine Learning Research*, pages 9558–9568. PMLR, 2021.
- [56] Martin Simonovsky and Nikos Komodakis. Graphvae: Towards generation of small graphs using variational autoencoders. In Vera Kurková, Yannis Manolopoulos, Barbara Hammer, Lazaros S. Iliadis, and Ilias Maglogiannis, editors, *Artificial Neural Networks and Machine Learning - ICANN 2018 - 27th International Conference on Artificial Neural Networks, Rhodes, Greece, October 4-7, 2018, Proceedings, Part I*, volume 11139 of *Lecture Notes in Computer Science*, pages 412–422. Springer, 2018.
- [57] Jascha Sohl-Dickstein, Eric A. Weiss, Niru Maheswaranathan, and Surya Ganguli. Deep unsupervised learning using nonequilibrium thermodynamics. In Francis R. Bach and David M. Blei, editors, *Proceedings of the 32nd International Conference on Machine Learning, ICML 2015, Lille, France, 6-11 July 2015*, volume 37 of *JMLR Workshop and Conference Proceedings*, pages 2256–2265. JMLR.org, 2015.
- [58] Yang Song and Stefano Ermon. Generative modeling by estimating gradients of the data distribution. In Hanna M. Wallach, Hugo Larochelle, Alina Beygelzimer, Florence d’Alché-Buc, Emily B. Fox, and Roman Garnett, editors, *Advances in Neural Information Processing Systems 32: Annual Conference on Neural Information Processing Systems 2019, NeurIPS 2019, December 8-14, 2019, Vancouver, BC, Canada*, pages 11895–11907, 2019.
- [59] Yang Song, Jascha Sohl-Dickstein, Diederik P. Kingma, Abhishek Kumar, Stefano Ermon, and Ben Poole. Score-based generative modeling through stochastic differential equations. In *9th International Conference on Learning Representations, ICLR 2021, Virtual Event, Austria, May 3-7, 2021*. OpenReview.net, 2021.
- [60] Haoran Sun, Lijun Yu, Bo Dai, Dale Schuurmans, and Hanjun Dai. Score-based continuous-time discrete diffusion models. In *The Eleventh International Conference on Learning Representations, ICLR 2023, Kigali, Rwanda, May 1-5, 2023*. OpenReview.net, 2023.
- [61] Clément Vignac and Pascal Frossard. Top-n: Equivariant set and graph generation without exchangeability. In *The Tenth International Conference on Learning Representations, ICLR 2022, Virtual Event, April 25-29, 2022*. OpenReview.net, 2022.
- [62] Clément Vignac, Igor Krawczuk, Antoine Siraudin, Bohan Wang, Volkan Cevher, and Pascal Frossard. Digress: Discrete denoising diffusion for graph generation. In *The Eleventh International Conference on Learning Representations, ICLR 2023, Kigali, Rwanda, May 1-5, 2023*. OpenReview.net, 2023.
- [63] Tomer Weiss, Eduardo Mayo Yanes, Sabyasachi Chakraborty, Luca Cosmo, Alex M Bronstein, and Renana Gershoni-Poranne. Guided diffusion for inverse molecular design. *Nature Computational Science*, 3(10):873–882, 2023.
- [64] Minkai Xu, Alexander S Powers, Ron O Dror, Stefano Ermon, and Jure Leskovec. Geometric latent diffusion models for 3d molecule generation. In *International Conference on Machine Learning*, pages 38592–38610. PMLR, 2023.
- [65] Minkai Xu, Lantao Yu, Yang Song, Chence Shi, Stefano Ermon, and Jian Tang. Geodiff: A geometric diffusion model for molecular conformation generation. In *The Tenth International Conference on Learning Representations, ICLR 2022, Virtual Event, April 25-29, 2022*. OpenReview.net, 2022.
- [66] Ling Yang, Zhilong Zhang, Yang Song, Shenda Hong, Runsheng Xu, Yue Zhao, Yingxia Shao, Wentao Zhang, Ming-Hsuan Yang, and Bin Cui. Diffusion models: A comprehensive survey of methods and applications. *CoRR*, abs/2209.00796, 2022.
- [67] Jiaxuan You, Jonathan Michael Gomes Selman, Rex Ying, and Jure Leskovec. Identity-aware graph neural networks. In *Thirty-Fifth AAAI Conference on Artificial Intelligence, AAAI 2021, Thirty-Third Conference on Innovative Applications of Artificial Intelligence, IAAI 2021, The Eleventh Symposium on Educational Advances in Artificial Intelligence, EAAI 2021, Virtual Event, February 2-9, 2021*, pages 10737–10745. AAAI Press, 2021.
- [68] Jiaxuan You, Rex Ying, Xiang Ren, William L. Hamilton, and Jure Leskovec. Graphrnn: Generating realistic graphs with deep auto-regressive models. In Jennifer G. Dy and Andreas Krause, editors, *Proceedings of the 35th International Conference on Machine Learning, ICML*

2018, *Stockholmsmässan, Stockholm, Sweden, July 10-15, 2018*, volume 80 of *Proceedings of Machine Learning Research*, pages 5694–5703. PMLR, 2018.

Appendix

The organization of this appendix is as follows

- Section A details the derivation of the factorized rate matrices.
- Section B details the forward transition probability matrix given a rate matrix.
- Section C includes all the proofs.
 - Section C.1: Proof of Proposition 3.2
 - Section C.2: Proof of Theorem 3.3
 - Section C.3: Proof of Lemma 3.5
 - Section C.4: Proof of Lemma 3.6
 - Section C.5: Proof of Lemma 3.7
 - Section C.6: Proof of Theorem 3.8
 - Section C.7: Proof of Theorem 3.9
- Section D includes a step-by-step sampling algorithm.
- Section E details the auxiliary features and neural modules used by DISCO.
- Section F includes detailed experimental settings and additional experimental results.
 - Section F.1: hardware and software
 - Section F.2: dataset setup
 - Section F.3: hyperparameter settings
 - Section F.4: additional effectiveness evaluation
 - Section F.5: convergence study
 - Section F.6: visualization
- Section G discusses this paper’s limitations and future work.

A Details of the Factorization of Rate Matrices

In this section, we detail the derivation of Remark 3.1, which is extended from the following Proposition 3 of [7].

Proposition A.1 (Factorization of the rate matrix, Proposition 3 from [7]). *If the forward process factorizes as $q_{t|s}(\mathbf{x}_t|\mathbf{x}_s) = \prod_{d=1}^D q_{t|s}(x_t^d|x_s^d)$, $t > s$, then the forward and reverse rates are of the form*

$$\mathbf{R}_t(\bar{\mathbf{x}}, \mathbf{x}) = \sum_{d=1}^D \mathbf{R}_t^d(\bar{x}^d, x^d) \delta_{\bar{\mathbf{x}} \setminus \bar{x}^d, \mathbf{x} \setminus x^d} \quad (13)$$

$$\tilde{\mathbf{R}}_t(\mathbf{x}, \bar{\mathbf{x}}) = \sum_{d=1}^D \mathbf{R}_t^d(\bar{x}^d, x^d) \delta_{\bar{\mathbf{x}} \setminus \bar{x}^d, \mathbf{x} \setminus x^d} \sum_{x_0^d} q_{0|t}(x_0^d|\mathbf{x}) \frac{q_{t|0}(\bar{x}^d|x_0^d)}{q_{t|0}(x^d|x_0^d)} \quad (14)$$

where $\delta_{\bar{\mathbf{x}} \setminus \bar{x}^d, \mathbf{x} \setminus x^d} = 1$ when all dimensions except for d are equal.

As all the nodes and edges are categorical, applying the above proposition of all the nodes and edges leads to our Remark 3.1.

B Details of Forward Transition Probability

In this section, we present the derivation of the forward transition probability for nodes; the forward process for edges can be derived similarly. Note that this derivation has been mentioned in [7] for generic discrete cases; we graft it to the graph settings and include it here for completeness. The core derivation of the forward transition probability is to prove the following proposition.

Proposition B.1 (Analytical forward process for commutable rate matrices, Proposition 10 from [7]). *if \mathbf{R}_t and $\mathbf{R}_{t'}$ commute $\forall t, t'$, $q_{t|0}(x_t = j|x_0 = i) = (e^{\int_0^t \mathbf{R}_s ds})_{ij}$*

Proof. If $q_{t|0} = \exp\left(\int_0^t \mathbf{R}_s ds\right)$ is the forward transition probability matrix, it should satisfy the Kolmogorov forward equation $\frac{d}{dt}q_{t|0} = q_{t|0}\mathbf{R}_t$. The transition probability matrix

$$q_{t|0} = \sum_{k=0}^{\infty} \frac{1}{k!} \left(\int_0^t \mathbf{R}_s ds\right)^k, \quad (15)$$

and, based on the fact that \mathbf{R}_t and $\mathbf{R}_{t'}$ commute $\forall t, t'$, its derivative is

$$\frac{d}{dt}q_{t|0} = \sum_{k=1}^{\infty} \frac{1}{(k-1)!} \left(\int_0^t \mathbf{R}_s ds\right)^{(k-1)} = q_{t|0}\mathbf{R}_t. \quad (16)$$

Thus, $q_{t|0} = \exp\left(\int_0^t \mathbf{R}_s ds\right)$ is the solution of Kolmogorov forward equation. \square

For the node i , if its forward rate matrix is set as $\mathbf{R}_t^i = \beta(t)\mathbf{R}_f$, we have \mathbf{R}_t^i and $\mathbf{R}_{t'}^i$ commute, $\forall t, t'$. Thus, the transition probability for node i is $q_{t|0}(f_t^i = v | f_0^i = u) = (e^{\int_0^t \beta(s)\mathbf{R}_f ds})_{uv}$. Based on similar derivation, we have the transition probability for the edge (i, j) as $q_{t|0}(e_t^{(i,j)} = v | e_0^{(i,j)} = u) = (e^{\int_0^t \beta(s)\mathbf{R}_e ds})_{uv}$.

C Proofs

C.1 Proof of Proposition 3.2

Proposition 3.2 claims the forward process converges to uniform distributions if $\mathbf{R}_f = \mathbf{1}\mathbf{1}^\top - b\mathbf{I}$ and $\mathbf{R}_e = \mathbf{1}\mathbf{1}^\top - (a+1)\mathbf{I}$ and it converges to marginal distributions \mathbf{m}_f and \mathbf{m}_e if $\mathbf{R}_f = \mathbf{1}\mathbf{m}_f^\top - \mathbf{I}$ and $\mathbf{R}_e = \mathbf{1}\mathbf{m}_e^\top - \mathbf{I}$.

Proof. If we formulate the rate matrices for nodes and edges as $\mathbf{R}_t^{(i,j)} = \beta(t)\mathbf{R}_e$, $\forall i, j$ and $\mathbf{R}_t^i = \beta(t)\mathbf{R}_f$, $\forall i$, every rate matrix is commutable for any time steps t and t' . In the following content, we show the proof for the node rate matrix $\mathbf{R}_t^i = \beta(t)\mathbf{R}_f$; the converged distribution of edge can be proved similarly. Based on Proposition B.1, the transition probability matrix between time steps t and $t + \Delta t$ is

$$q_{t+\Delta t|t} = \mathbf{I} + \int_t^{t+\Delta t} \beta(s)\mathbf{R}_f ds + O((\Delta t)^2) \quad (17)$$

$$= \mathbf{I} + \Delta t\beta(\xi)\mathbf{R}_f + O((\Delta t)^2), \quad (18)$$

where the second line we use the Mean Value Theorem. If the high-order term $O((\Delta t)^2)$ is omitted and we short $\beta_{\Delta t} = \Delta t\beta(\xi)$, for $\mathbf{R}_f = \mathbf{1}\mathbf{1}^\top - b\mathbf{I}$, we have

$$q_{t+\Delta t|t} \approx \beta_{\Delta t}\mathbf{1}\mathbf{1}^\top + (1 - \beta_{\Delta t}b)\mathbf{I}, \quad (19)$$

which is the transition matrix of the uniform diffusion in the discrete-time diffusion models [57, 2]. Thus, with $T \rightarrow \infty$ and $q_{t+\Delta t|t}$ to the power of infinite, the converged distribution is a uniform distribution. Similarly, for $\mathbf{R}_f = \mathbf{1}\mathbf{m}_f^\top - \mathbf{I}$ the transition matrix is

$$q_{t+\Delta t|t} \approx \beta_{\Delta t}\mathbf{1}\mathbf{m}_f^\top + (1 - \beta_{\Delta t})\mathbf{I} \quad (20)$$

which is a generalized transition matrix of the ‘absorbing state’ diffusion [2]. The difference lies at for the ‘absorbing state’ diffusion [2], \mathbf{m}_f is set as a one-hot vector for the absorbing state, and here we set it as the marginal distribution. Thus, with $T \rightarrow \infty$ and $q_{t+\Delta t|t}$ to the power of infinite, the converged distribution is a marginal distribution \mathbf{m}_f . \square

C.2 Proof of Theorem 3.3

Theorem 3.3 says for $\mathcal{G} \neq \bar{\mathcal{G}}$,

$$\begin{aligned} \left| \tilde{\mathbf{R}}_t(\mathcal{G}, \bar{\mathcal{G}}) - \tilde{\mathbf{R}}_{\theta,t}(\mathcal{G}, \bar{\mathcal{G}}) \right|^2 &\leq C_t + C_t^{\text{node}} \mathbb{E}_{\mathcal{G}_0} q_{t|0}(\mathcal{G}|\mathcal{G}_0) \sum_i \mathcal{L}_{\text{CE}}(\text{One-Hot}(f_0^i), \hat{f}_0^i) \\ &\quad + C_t^{\text{edge}} \mathbb{E}_{\mathcal{G}_0} q_{t|0}(\mathcal{G}|\mathcal{G}_0) \sum_{i,j} \mathcal{L}_{\text{CE}}(\text{One-Hot}(e_0^{(i,j)}), \hat{e}_0^{(i,j)}) \end{aligned} \quad (21)$$

where the node and edge estimated probability vector (sum is 1) is notated as $\hat{f}_0^i = [p_{0|t}^\theta(f^i = 1|\mathcal{G}_t), \dots, p_{0|t}^\theta(f^i = b|\mathcal{G}_t)]^\top \in [0, 1]^b$ and $\hat{e}_0^{(i,j)} = [p_{0|t}^\theta(e^{(i,j)} = 1|\mathcal{G}_t), \dots, p_{0|t}^\theta(e^{(i,j)} = a+1|\mathcal{G}_t)]^\top \in [0, 1]^{a+1}$.

Proof.

$$\begin{aligned} &\left| \tilde{\mathbf{R}}_t(\mathcal{G}, \bar{\mathcal{G}}) - \tilde{\mathbf{R}}_{\theta,t}(\mathcal{G}, \bar{\mathcal{G}}) \right| \quad (22) \\ &= \left| \sum_i A_t^i \sum_{f_0^i} \frac{q_{t|0}(\bar{f}^i|f_0^i)}{q_{t|0}(f^i|f_0^i)} (q_{0|t}(f_0^i|\mathcal{G}) - p_{0|t}^\theta(f_0^i|\mathcal{G})) \right. \end{aligned}$$

$$\left. + \sum_{i,j} B_t^{(i,j)} \sum_{e_0^{(i,j)}} \frac{q_{t|0}(\bar{e}^{(i,j)}|e_0^{(i,j)})}{q_{t|0}(e^{(i,j)}|e_0^{(i,j)})} (q_{0|t}(e_0^{(i,j)}|\mathcal{G}) - p_{0|t}^\theta(e_0^{(i,j)}|\mathcal{G})) \right| \quad (23)$$

$$\begin{aligned} &\leq \left| \sum_i A_t^i \sum_{f_0^i} \frac{q_{t|0}(\bar{f}^i|f_0^i)}{q_{t|0}(f^i|f_0^i)} (q_{0|t}(f_0^i|\mathcal{G}) - p_{0|t}^\theta(f_0^i|\mathcal{G})) \right| \\ &\quad + \left| \sum_{i,j} B_t^{(i,j)} \sum_{e_0^{(i,j)}} \frac{q_{t|0}(\bar{e}^{(i,j)}|e_0^{(i,j)})}{q_{t|0}(e^{(i,j)}|e_0^{(i,j)})} (q_{0|t}(e_0^{(i,j)}|\mathcal{G}) - p_{0|t}^\theta(e_0^{(i,j)}|\mathcal{G})) \right| \end{aligned} \quad (24)$$

We check the first term of Eq. (24):

$$\left| \sum_i A_t^i \sum_{f_0^i} \frac{q_{t|0}(\bar{f}^i|f_0^i)}{q_{t|0}(f^i|f_0^i)} (q_{0|t}(f_0^i|\mathcal{G}) - p_{0|t}^\theta(f_0^i|\mathcal{G})) \right| \quad (25)$$

$$\leq \sum_i A_t^i \sup_{f_0^i} \left\{ \frac{q_{t|0}(\bar{f}^i|f_0^i)}{q_{t|0}(f^i|f_0^i)} \right\} \sum_{f_0^i} \left| q_{0|t}(f_0^i|\mathcal{G}) - p_{0|t}^\theta(f_0^i|\mathcal{G}) \right| \quad (26)$$

$$= \sum_i C_i \sum_{f_0^i} \left| q_{0|t}(f_0^i|\mathcal{G}) - p_{0|t}^\theta(f_0^i|\mathcal{G}) \right| \quad (27)$$

$$\stackrel{(*)}{\leq} \sum_i C_i \sqrt{2 \sum_{f_0^i} \left(C_{f_0^i} - q_{0|t}(f_0^i|\mathcal{G}) \log p_{0|t}^\theta(f_0^i|\mathcal{G}) \right)} \quad (28)$$

$$\stackrel{(**)}{\leq} C_1 \sqrt{\sum_i \sum_{f_0^i} \left(C_{f_0^i} - q_{0|t}(f_0^i|\mathcal{G}) \log p_{0|t}^\theta(f_0^i|\mathcal{G}) \right)} \quad (29)$$

$$= C_1 \sqrt{C_2 - \sum_i \sum_{f_0^i} q_{0|t}(f_0^i|\mathcal{G}) \log p_{0|t}^\theta(f_0^i|\mathcal{G})} \quad (30)$$

where $C_i = A_t^i \sup_{f_0^i} \left\{ \frac{q_{t|0}(\bar{f}^i|f_0^i)}{q_{t|0}(f^i|f_0^i)} \right\}$, $C_{f_0^i} = q_{0|t}(f_0^i|\mathcal{G}) \log q_{0|t}(f_0^i|\mathcal{G})$, (*) is based on the Pinsker's inequality, (**) is based on Cauchy-Schwarz inequality: $\sum_{i=1}^n \sqrt{x_i} \leq \sqrt{n \sum_{i=1}^n x_i}$, $C_1 = \sqrt{2n} \sup_i \{C_i\}$, $C_2 = \sum_i \sum_{f_0^i} C_{f_0^i}$. Next, the term $-\sum_i \sum_{f_0^i} q_{0|t}(f_0^i|\mathcal{G}) \log p_{0|t}^\theta(f_0^i|\mathcal{G})$ is equiva-

lent to:

$$- \sum_i \sum_{f_0^i} q_{0|t}(f_0^i | \mathcal{G}) \log p_{0|t}^\theta(f_0^i | \mathcal{G}) \quad (31)$$

$$= - \frac{1}{p_t(\mathcal{G})} \sum_i \sum_{f_0^i} p_{0,t}(f_0^i, \mathcal{G}) \log p_{0|t}^\theta(f_0^i | \mathcal{G}) \quad (32)$$

$$= - \frac{1}{p_t(\mathcal{G})} \sum_i \sum_{f_0^i} \sum_{\mathcal{G}_0(f_0^i)} p_{0,t}(\mathcal{G}_0, \mathcal{G}) \log p_{0|t}^\theta(f_0^i | \mathcal{G}) \quad (33)$$

$$= - \frac{1}{p_t(\mathcal{G})} \sum_i \sum_{f_0^i} \sum_{\mathcal{G}_0(f_0^i)} \pi_{\text{data}}(\mathcal{G}_0) q_{t|0}(\mathcal{G} | \mathcal{G}_0) \log p_{0|t}^\theta(f_0^i | \mathcal{G}) \quad (34)$$

$$= \frac{1}{p_t(\mathcal{G})} \sum_i \sum_{f_0^i} \sum_{\mathcal{G}_0(f_0^i)} \pi_{\text{data}}(\mathcal{G}_0) q_{t|0}(\mathcal{G} | \mathcal{G}_0) \mathcal{L}_{\text{CE}}(\text{One-Hot}(f_0^i), \hat{f}_0^i) \quad (35)$$

$$= \frac{1}{p_t(\mathcal{G})} \sum_{\mathcal{G}_0} \pi_{\text{data}}(\mathcal{G}_0) q_{t|0}(\mathcal{G} | \mathcal{G}_0) \sum_i \mathcal{L}_{\text{CE}}(\text{One-Hot}(f_0^i), \hat{f}_0^i) \quad (36)$$

$$= \frac{1}{p_t(\mathcal{G})} \mathbb{E}_{\mathcal{G}_0} q_{t|0}(\mathcal{G} | \mathcal{G}_0) \sum_i \mathcal{L}_{\text{CE}}(\text{One-Hot}(f_0^i), \hat{f}_0^i) \quad (37)$$

where $\sum_{\mathcal{G}_0(f_0^i)}$ marginalizing all the graphs at time 0 whose i -th node is f_0^i ; $p_{0,t}(f_0^i, \mathcal{G})$ is the joint probability of a graph whose i -th node is f_0^i at time 0 and it is \mathcal{G} at time t ; $p_{0,t}(\mathcal{G}_0, \mathcal{G})$ is the joint probability of a graph which is \mathcal{G}_0 at time 0 and it is \mathcal{G} at time t . Plugging Eq. (37) into Eq. (30):

$$\begin{aligned} & \left| \sum_i A_t \sum_{f_0^i} \frac{q_{t|0}(\bar{f}^i | f_0^i)}{q_{t|0}(f^i | f_0^i)} (q_{0|t}(f_0^i | \mathcal{G}) - p_{0|t}^\theta(f_0^i | \mathcal{G})) \right| \\ & \leq C_1 \sqrt{C_2 + C_5 \mathbb{E}_{\mathcal{G}_0} q_{t|0}(\mathcal{G} | \mathcal{G}_0) \sum_i \mathcal{L}_{\text{CE}}(\text{One-Hot}(f_0^i), \hat{f}_0^i)} \end{aligned} \quad (38)$$

where $C_5 = \frac{1}{p_t(\mathcal{G})}$. A similar analysis can be conducted about the second term of Eq. (24) and we directly present it here:

$$\begin{aligned} & \left| \sum_{i,j} B_t^{(i,j)} \sum_{e_0^{(i,j)}} \frac{q_{t|0}(\bar{e}^{(i,j)} | e_0^{(i,j)})}{q_{t|0}(e^{(i,j)} | e_0^{(i,j)})} (q_{0|t}(e_0^{(i,j)} | \mathcal{G}) - p_{0|t}^\theta(e_0^{(i,j)} | \mathcal{G})) \right| \\ & \leq C_3 \sqrt{C_4 + C_5 \mathbb{E}_{\mathcal{G}_0} q_{t|0}(\mathcal{G} | \mathcal{G}_0) \sum_{i,j} \mathcal{L}_{\text{CE}}(\text{One-Hot}(e_0^{(i,j)}), \hat{e}_0^{(i,j)})} \end{aligned} \quad (39)$$

where $C_3 = \sqrt{2n} \sup_{i,j} \{C_{i,j}\}$, $C_4 = \sum_{i,j} \sum_{e_0^{(i,j)}} C_{e_0^{(i,j)}}$, $C_{i,j} = B_t^{(i,j)} \sup_{e_0^{(i,j)}} \left\{ \frac{q_{t|0}(\bar{e}^{(i,j)} | e_0^{(i,j)})}{q_{t|0}(e^{(i,j)} | e_0^{(i,j)})} \right\}$, $C_{e_0^{(i,j)}} = q_{0|t}(e_0^{(i,j)} | \mathcal{G}) \log q_{0|t}(e_0^{(i,j)} | \mathcal{G})$.

Plugging Eqs. (38) and (39) into Eq. (24), being aware that C_1, C_2, C_3, C_4, C_5 are all t -related:

$$\begin{aligned} \left| \tilde{\mathbf{R}}_t(\mathcal{G}, \bar{\mathcal{G}}) - \tilde{\mathbf{R}}_{\theta,t}(\mathcal{G}, \bar{\mathcal{G}}) \right| & \leq C_1 \sqrt{C_2 + C_5 \mathbb{E}_{\mathcal{G}_0} q_{t|0}(\mathcal{G} | \mathcal{G}_0) \sum_i \mathcal{L}_{\text{CE}}(\text{One-Hot}(f_0^i), \hat{f}_0^i)} \\ & + C_3 \sqrt{C_4 + C_5 \mathbb{E}_{\mathcal{G}_0} q_{t|0}(\mathcal{G} | \mathcal{G}_0) \sum_{i,j} \mathcal{L}_{\text{CE}}(\text{One-Hot}(e_0^{(i,j)}), \hat{e}_0^{(i,j)})} \end{aligned} \quad (40)$$

$$\begin{aligned} & \stackrel{(*)}{\leq} \left(C_t + C_t^{\text{node}} \mathbb{E}_{\mathcal{G}_0} q_{t|0}(\mathcal{G} | \mathcal{G}_0) \sum_i \mathcal{L}_{\text{CE}}(\text{One-Hot}(f_0^i), \hat{f}_0^i) \right. \\ & \left. + C_t^{\text{edge}} \mathbb{E}_{\mathcal{G}_0} q_{t|0}(\mathcal{G} | \mathcal{G}_0) \sum_{i,j} \mathcal{L}_{\text{CE}}(\text{One-Hot}(e_0^{(i,j)}), \hat{e}_0^{(i,j)}) \right)^{1/2} \end{aligned} \quad (41)$$

where (*) is based on Cauchy–Schwarz inequality, $C_t = 2C_1^2C_2 + 2C_3^2C_4$, $C_t^{\text{node}} = 2C_1^2C_5$, $C_t^{\text{edge}} = 2C_3^2C_5$. \square

C.3 Proof of Lemma 3.5

We clarify that the term "permutation" in this paper refers to the reordering of the node indices, i.e., the first dimension of \mathbf{F} and the first two dimensions of \mathbf{E} .

Proof. The input of an MPNN layer is $\mathbf{F} = \{\mathbf{r}_i\}_{i=1}^n \in \mathbb{R}^{n \times d}$, $\mathbf{E} = \{\mathbf{r}_{i,j}\}_{i,j=1}^n \in \mathbb{R}^{n \times n \times d}$, $\mathbf{y} \in \mathbb{R}^d$, where d is the hidden dimension. The updating formulas of an MPNN layer can be presented as

$$\mathbf{r}^i \leftarrow \text{FiLM}\left(\text{FiLM}\left(\mathbf{r}^i, \text{MLP}\left(\frac{\sum_{j=1}^n \mathbf{r}^{(j,i)}}{n}\right)\right), \mathbf{y}\right), \quad (42)$$

$$\mathbf{r}^{(i,j)} \leftarrow \text{FiLM}(\text{FiLM}(\mathbf{r}^{(i,j)}, \mathbf{r}^i \odot \mathbf{r}^j), \mathbf{y}), \quad (43)$$

$$\mathbf{y} \leftarrow \mathbf{y} + \text{PNA}(\{\mathbf{r}^i\}_{i=1}^n) + \text{PNA}(\{\mathbf{r}^{(i,j)}\}_{i,j=1}^n), \quad (44)$$

The permutation \mathcal{P} of the input of an MPNN layer can be presented as $\mathcal{P}(\mathbf{F} = \{\mathbf{r}_i\}_{i=1}^n, \mathbf{E} = \{\mathbf{r}_{i,j}\}_{i,j=1}^n, \mathbf{y}) = (\{\mathbf{r}_{\sigma(i)}\}_{i=1}^n, \{\mathbf{r}_{\sigma(i),\sigma(j)}\}_{i,j=1}^n, \mathbf{y})$ where $\sigma : \{1, \dots, n\} \mapsto \{1, \dots, n\}$ is a bijection.

For PNA (Eq. (74)), it includes operations \max , \min , mean , and std which are all permutation-invariant and thus, the PNA module is permutation-invariant. Then,

$$\mathbf{y} + \text{PNA}(\{\mathbf{r}^i\}_{i=1}^n) + \text{PNA}(\{\mathbf{r}^{(i,j)}\}_{i,j=1}^n) = \mathbf{y} + \text{PNA}(\{\mathbf{r}^{\sigma(i)}\}_{i=1}^n) + \text{PNA}(\{\mathbf{r}^{(\sigma(i),\sigma(j))}\}_{i,j=1}^n) \quad (45)$$

Because $\sum_{j=1}^n \mathbf{r}_{j,i} = \sum_{j=1}^n \mathbf{r}_{\sigma(j),\sigma(i)}$, $\mathbf{r}_i \odot \mathbf{r}_j = \mathbf{r}_{\sigma(i)} \odot \mathbf{r}_{\sigma(j)}$, and the FiLM module (Eq. (75)) is not related to the node ordering,

$$\mathbf{r}^{(\sigma(i),\sigma(j))} \leftarrow \text{FiLM}(\text{FiLM}(\mathbf{r}^{(\sigma(i),\sigma(j))}, \mathbf{r}^{\sigma(i)} \odot \mathbf{r}^{\sigma(j)}), \mathbf{y}) = \text{FiLM}(\text{FiLM}(\mathbf{r}^{(i,j)}, \mathbf{r}^i \odot \mathbf{r}^j), \mathbf{y}) \quad (46)$$

$$\mathbf{r}^{\sigma(i)} \leftarrow \text{FiLM}\left(\text{FiLM}\left(\mathbf{r}^{\sigma(i)}, \text{MLP}\left(\frac{\sum_{j=1}^n \mathbf{r}^{(\sigma(j),\sigma(i))}}{n}\right)\right), \mathbf{y}\right) \quad (47)$$

$$= \text{FiLM}\left(\text{FiLM}\left(\mathbf{r}^i, \text{MLP}\left(\frac{\sum_{j=1}^n \mathbf{r}^{(j,i)}}{n}\right)\right), \mathbf{y}\right) \quad (48)$$

Thus, we proved that

$$\text{MPNN}\left(\mathcal{P}(\mathbf{F}, \mathbf{E}, \mathbf{y})\right) = \mathcal{P}\left(\text{MPNN}(\mathbf{F}, \mathbf{E}, \mathbf{y})\right) \quad (49)$$

\square

C.4 Proof of Lemma 3.6

Proof. The forward rate matrix (Eq. (5)) is the sum of component-specific forward rate matrices ($\{\mathbf{R}_t^{(i,j)}\}_{i,j \in \mathbb{N}_{\leq n}^+}$ and $\{\mathbf{R}_t^i\}_{i \in \mathbb{N}_{\leq n}^+}$). It is permutation-invariant because the summation is permutation-invariant.

The parametric reverse rate matrix is

$$\tilde{\mathbf{R}}_{\theta,t}(\mathcal{G}, \bar{\mathcal{G}}) = \sum_i \tilde{\mathbf{R}}_{\theta,t}^i(f^i, \bar{f}^i) + \sum_{i,j} \tilde{\mathbf{R}}_{\theta,t}^{(i,j)}(e^{(i,j)}, \bar{e}^{(i,j)}) \quad (50)$$

where $\tilde{\mathbf{R}}_{\theta,t}^i(f^i, \bar{f}^i) = A_t^i \sum_{f_0^i} \frac{q_{t|0}(\bar{f}^i | f_0^i)}{q_{t|0}(f^i | \bar{f}_0^i)} p_{0|t}^\theta(f_0^i | \mathcal{G}_t)$, $\tilde{\mathbf{R}}_{\theta,t}^{(i,j)}(e^{(i,j)}, \bar{e}^{(i,j)}) = B_t^{(i,j)} \sum_{e_0^{(i,j)}} \frac{q_{t|0}(\bar{e}^{(i,j)} | e_0^{(i,j)})}{q_{t|0}(e^{(i,j)} | \bar{e}_0^{(i,j)})} p_{0|t}^\theta(e_0^{(i,j)} | \mathcal{G}_t)$. If we present the permutation \mathcal{P} on every node

as a bijection $\sigma : \{1, \dots, n\} \mapsto \{1, \dots, n\}$, the term

$$\tilde{\mathbf{R}}_{\theta,t}^i(f^i, \bar{f}^i) = A_t^i \sum_{f_0^i} \frac{q_{t|0}(f^i|f_0^i)}{q_{t|0}(f^i|f_0^i)} p_{0|t}^\theta(f_0^i|\mathcal{G}_t) \quad (51)$$

$$= \mathbf{R}_t^i(\bar{f}^i, f^i) \delta_{\bar{\mathcal{G}} \setminus \bar{f}^i, \mathcal{G} \setminus f^i} \sum_{f_0^i} \frac{q_{t|0}(\bar{f}^i|f_0^i)}{q_{t|0}(f^i|f_0^i)} p_{0|t}^\theta(f_0^i|\mathcal{G}_t) \quad (52)$$

$$\stackrel{(*)}{=} \mathbf{R}_t^{\sigma(i)}(\bar{f}^{\sigma(i)}, f^{\sigma(i)}) \delta_{\mathcal{P}(\bar{\mathcal{G}}) \setminus \bar{f}^{\sigma(i)}, \mathcal{P}(\mathcal{G}) \setminus f^{\sigma(i)}} \sum_{f_0^{\sigma(i)}} \frac{q_{t|0}(\bar{f}^{\sigma(i)}|f_0^{\sigma(i)})}{q_{t|0}(f^{\sigma(i)}|f_0^{\sigma(i)})} p_{0|t}^\theta(f_0^{\sigma(i)}|\mathcal{G}_t) \quad (53)$$

$$\stackrel{(**)}{=} \mathbf{R}_t^{\sigma(i)}(\bar{f}^{\sigma(i)}, f^{\sigma(i)}) \delta_{\mathcal{P}(\bar{\mathcal{G}}) \setminus \bar{f}^{\sigma(i)}, \mathcal{P}(\mathcal{G}) \setminus f^{\sigma(i)}} \sum_{f_0^{\sigma(i)}} \frac{q_{t|0}(\bar{f}^{\sigma(i)}|f_0^{\sigma(i)})}{q_{t|0}(f^{\sigma(i)}|f_0^{\sigma(i)})} p_{0|t}^\theta(f_0^{\sigma(i)}|\mathcal{P}(\mathcal{G}_t)) \quad (54)$$

$$= \tilde{\mathbf{R}}_{\theta,t}^{\sigma(i)}(f^{\sigma(i)}, \bar{f}^{\sigma(i)}) \quad (55)$$

where (*) is based on the permutation invariant of the forward process and its rate matrix and (**) is based on the permutation equivariance of the graph-to-graph backbone $p_{0|t}^\theta$. \square

C.5 Proof of Lemma 3.7

Recall the Kolmogorov forward equation, for $s < t$,

$$\frac{d}{dt} q_{t|s}(\mathbf{x}_t|\mathbf{x}_s) = \sum_{\xi \in \mathcal{X}} q_{t|s}(\xi|\mathbf{x}_s) \mathbf{R}_t(\xi, \mathbf{x}_t). \quad (56)$$

Proof. We aim to show that $q_{t|s}(\mathcal{P}(\mathbf{x}_t)|\mathcal{P}(\mathbf{x}_s))$ is a solution of Eq. (56). Because the permutation \mathcal{P} is a bijection, we have

$$\frac{d}{dt} q_{t|s}(\mathcal{P}(\mathbf{x}_t)|\mathcal{P}(\mathbf{x}_s)) \quad (57)$$

$$= \sum_{\xi \in \mathcal{X}} q_{t|s}(\mathcal{P}(\xi)|\mathcal{P}(\mathbf{x}_s)) \mathbf{R}_t(\mathcal{P}(\xi), \mathcal{P}(\mathbf{x}_t)) \quad (58)$$

$$\stackrel{(*)}{=} \sum_{\xi \in \mathcal{X}} q_{t|s}(\mathcal{P}(\xi)|\mathcal{P}(\mathbf{x}_s)) \mathbf{R}_t(\xi, \mathbf{x}_t) \quad (59)$$

where (*) is because \mathbf{R}_t is permutation-invariant. As Eq. 59 and Eq. 56 share the same rate matrix, and the rate matrix completely determines the CTMC (and its Kolmogorov forward equation) [53], thus, their solutions are the same: $q_{t|s}(\mathbf{x}_t|\mathbf{x}_s) = q_{t|s}(\mathcal{P}(\mathbf{x}_t)|\mathcal{P}(\mathbf{x}_s))$, i.e., the transition probability is permutation-invariant. \square

C.6 Proof of Theorem 3.8

Proof. We start from a simple case where the parametric rate matrix is fixed all the time,

$$p_0^\theta(\mathcal{G}_0) = \sum_{\mathcal{G}_T} q_{0|T}^\theta(\mathcal{G}_0|\mathcal{G}_T) \pi_{\text{ref}}(\mathcal{G}_T), \quad (60)$$

where the transition probability is by solving the Kolmogorov forward equation

$$\frac{d}{dt} q_{t|s}^\theta(\mathcal{G}_t|\mathcal{G}_s) = \sum_{\xi} q_{t|s}^\theta(\xi|\mathcal{G}_s) \tilde{\mathbf{R}}_\theta(\xi, \mathcal{G}_t). \quad (61)$$

Thus, the sampling probability of permuted graph $\mathcal{P}(\mathcal{G}_0)$

$$p_0^\theta(\mathcal{P}(\mathcal{G}_0)) = \sum_{\mathcal{G}_T} q_{0|T}^\theta(\mathcal{P}(\mathcal{G}_0)|\mathcal{P}(\mathcal{G}_T))\pi_{\text{ref}}(\mathcal{P}(\mathcal{G}_T)) \quad (62)$$

$$\stackrel{(*)}{=} \sum_{\mathcal{G}_T} q_{0|T}^\theta(\mathcal{G}_0|\mathcal{G}_T)\pi_{\text{ref}}(\mathcal{P}(\mathcal{G}_T)) \quad (63)$$

$$\stackrel{(**)}{=} \sum_{\mathcal{G}_T} q_{0|T}^\theta(\mathcal{G}_0|\mathcal{G}_T)\pi_{\text{ref}}(\mathcal{G}_T) \quad (64)$$

$$= p_0^\theta(\mathcal{G}_0) \quad (65)$$

where (*) is based on Lemma 3.6 and Lemma 3.7, the transition probability of DISCO is permutation-invariant and (**) is from the assumption that the reference distribution $\pi_{\text{ref}}(\mathcal{G}_T)$ is permutation-invariant. Thus, we proved that for the simple case, $\tilde{\mathbf{R}}_{\theta,t}$ fixed $\forall t$, the sampling probability is permutation-invariant.

For the practical sampling, as we mentioned in Section 3.4, the τ -leaping algorithm assumes that the time interval $[0, T]$ is divided into various length- τ intervals $[0, \tau), [\tau, 2\tau), \dots, [T - \tau, T]$ (here both close sets or open sets work) and assume the reverse rate matrix is fixed as $\tilde{\mathbf{R}}_{\theta,t}$ within every length- τ interval, such as $(t - \tau, t]$. Thus, the sampling probability can be computed as

$$p_0^\theta(\mathcal{G}_0) = \sum_{\mathcal{G}_T, \mathcal{G}_{T-\tau}, \dots, \mathcal{G}_\tau} q_{0|\tau}(\mathcal{G}_0|\mathcal{G}_\tau) \cdots q_{T-\tau|T}(\mathcal{G}_{T-\tau}|\mathcal{G}_T)\pi_{\text{ref}}(\mathcal{G}_T). \quad (66)$$

The conclusion from the simple case can be generalized to this τ -leaping-based case because all the transition probability $q_{t-\tau|t}(\mathcal{G}_{t-\tau}|\mathcal{G}_t)$ and the reference distribution are permutation-invariant. \square

Note that Xu et al. [65] have a similar analysis in their Proposition 1 on a DDPM-based model.

C.7 Proof of Theorem 3.9

Recall our training objective is

$$\min_{\theta} T\mathbb{E}_{t \sim \mathcal{U}_{(0,T)}} \mathbb{E}_{\mathcal{G}_0} \mathbb{E}_{q_{t|0}(\mathcal{G}_t|\mathcal{G}_0)} \left[\sum_i \mathcal{L}_{\text{CE}}(\text{One-Hot}(f_0^i), \hat{f}_0^i) + \sum_{i,j} \mathcal{L}_{\text{CE}}(\text{One-Hot}(e_0^{(i,j)}), \hat{e}_0^{(i,j)}) \right] \quad (67)$$

where $\hat{f}_0^i = [p_{0|t}^\theta(f^i = 1|\mathcal{G}_t), \dots, p_{0|t}^\theta(f^i = b|\mathcal{G}_t)]^\top \in [0, 1]^b$ and $\hat{e}_0^{(i,j)} = [p_{0|t}^\theta(e^{(i,j)} = 1|\mathcal{G}_t), \dots, p_{0|t}^\theta(e^{(i,j)} = a+1|\mathcal{G}_t)]^\top \in [0, 1]^{a+1}$

Proof. We follow the notation and present the permutation \mathcal{P} on every node as a bijection $\sigma : \{1, \dots, n\} \mapsto \{1, \dots, n\}$. We first analyze the cross-entropy loss on the nodes for a single training graph \mathcal{G}_0

$$\mathcal{L}_{\text{node}}(\mathcal{G}_0) = T\mathbb{E}_{t \sim \mathcal{U}_{(0,T)}} \mathbb{E}_{q_{t|0}(\mathcal{G}_t|\mathcal{G}_0)} \sum_i \mathcal{L}_{\text{CE}}(\text{One-Hot}(f_0^i), \hat{f}_0^i) \quad (68)$$

$$= T\mathbb{E}_{t \sim \mathcal{U}_{(0,T)}} \sum_{\mathcal{G}_t} q_{t|0}(\mathcal{G}_t|\mathcal{G}_0) \sum_i \mathcal{L}_{\text{CE}}(\text{One-Hot}(f_0^i), \hat{f}_0^i) \quad (69)$$

$$\stackrel{(*)}{=} T\mathbb{E}_{t \sim \mathcal{U}_{(0,T)}} \sum_{\mathcal{G}_t} q_{t|0}(\mathcal{P}(\mathcal{G}_t)|\mathcal{P}(\mathcal{G}_0)) \sum_i \mathcal{L}_{\text{CE}}(\text{One-Hot}(f_0^i), \hat{f}_0^i) \quad (70)$$

$$\stackrel{(**)}{=} T\mathbb{E}_{t \sim \mathcal{U}_{(0,T)}} \sum_{\mathcal{G}_t} q_{t|0}(\mathcal{P}(\mathcal{G}_t)|\mathcal{P}(\mathcal{G}_0)) \sum_i \mathcal{L}_{\text{CE}}(\text{One-Hot}(f_0^{\sigma(i)}), \hat{f}_0^{\sigma(i)}) \quad (71)$$

$$= \mathcal{L}_{\text{node}}(\mathcal{P}(\mathcal{G}_0)) \quad (72)$$

where (*) is from the permutation invariance of the forward process and (**) is from the permutation equivariance of the graph-to-graph backbone and the permutation invariance of the cross-entropy

loss. A similar result can be analyzed on the cross-entropy loss on the edges

$$\mathcal{L}_{\text{edge}}(\mathcal{G}_0) = T \mathbb{E}_{t \sim \mathcal{U}(0, T)} \mathbb{E}_{q_t | 0}(\mathcal{G}_t | \mathcal{G}_0) \sum_{i, j} \mathcal{L}_{\text{CE}}(\text{One-Hot}(e_0^{(i, j)}), \hat{e}_0^{(i, j)}) = \mathcal{L}_{\text{edge}}(\mathcal{P}(\mathcal{G}_0)) \quad (73)$$

and we omit the proof here for brevity. \square

D Sampling Algorithm

A Step-by-step procedure about the τ -leaping graph generation is presented in Algorithm 2.

Algorithm 2 τ -Leaping Graph Generation

```

1:  $t \leftarrow T$ 
2:  $\mathcal{G}_t = (\{e^{(i, j)}\}_{i, j \in \mathbb{N}_{\leq n}^+}, \{f^i\}_{i \in \mathbb{N}_{\leq n}^+}) \leftarrow \pi_{\text{ref}}(\mathcal{G})$ 
3: while  $t > 0$  do
4:   for  $i = 1, \dots, n$  do
5:     for  $s = 1, \dots, b$  do
6:        $\tilde{\mathbf{R}}_{\theta, t}^i(f^i, s) = \mathbf{R}_t^i(s, f^i) \sum_{f_0^i} \frac{q_{t|0}(s|f_0^i)}{q_{t|0}(f^i|f_0^i)} p_{\theta}(f^i | \mathcal{G}_t, t)$ 
7:        $J_{f^i, s} \leftarrow \text{Poisson}(\tau \tilde{\mathbf{R}}_t^i(s, f^i))$   $\triangleright$  # of transition for every edge
8:     end for
9:   end for
10:  for  $i, j = 1, \dots, n$  do
11:    for  $s = 1, \dots, a$  do
12:       $\tilde{\mathbf{R}}_{\theta, t}^{(i, j)}(e^{(i, j)}, s) = \mathbf{R}_t^{(i, j)}(s, e^{(i, j)}) \sum_{e_0^{(i, j)}} \frac{q_{t|0}(s|e_0^{(i, j)})}{q_{t|0}(e^{(i, j)}|e_0^{(i, j)})} p_{\theta}(e^{(i, j)} | \mathcal{G}_t, t)$ 
13:       $J_{e^{(i, j)}, s} \leftarrow \text{Poisson}(\tau \tilde{\mathbf{R}}_t^{(i, j)}(s, e^{(i, j)}))$   $\triangleright$  # of transition for every edge
14:    end for
15:  end for
16:  for  $i = 1, \dots, n$  do
17:    if  $\sum_{s=1}^b J_{f^i, s} > 1$  or  $\sum_{s=1}^b J_{f^i, s} = 0$  then
18:       $f^i \leftarrow f^i$   $\triangleright$  stay the same
19:    else
20:       $s^* = \arg \max_s \{J_{f^i, s}\}_{s=1}^b$ 
21:       $f^i \leftarrow s^*$   $\triangleright$  update node
22:    end if
23:  end for
24:  for  $i, j = 1, \dots, n$  do
25:    if  $\sum_{s=1}^a J_{e^{(i, j)}, s} > 1$  or  $\sum_{s=1}^a J_{e^{(i, j)}, s} = 0$  then
26:       $e^{(i, j)} \leftarrow e^{(i, j)}$   $\triangleright$  stay the same
27:    else
28:       $s^* = \arg \max_s \{J_{e^{(i, j)}, s}\}_{s=1}^a$ 
29:       $e^{(i, j)} \leftarrow s^*$   $\triangleright$  update edge
30:    end if
31:  end for
32:   $t \leftarrow t - \tau$ 
33: end while

```

E Auxiliary Features and Implementation Details

For learning a better graph-to-graph mapping $p_{0|t}^{\theta}(\mathcal{G}_0 | \mathcal{G}_t)$, artificially augmenting the node-level features and graph-level features is proved effective to enhance the expressiveness of graph learning models [67, 62]. For this setting, we keep consistent with the state-of-the-art model, DiGress [62], and extract the following three sets of auxiliary features. Note that the following features are extracted on the noised graph \mathcal{G}_t .

We binarize the edge tensor \mathbf{E} into an adjacency matrix $\mathbf{A} \in \{0, 1\}^{n \times n}$ whose 1 entries denote the corresponding node pair is connected by any type of edge.

Motif features. The number of length-3/4/5 cycles every node is included in is counted as the topological node-level features; also, the total number of length-3/4/5/6 cycles is the topological graph-level features.

Spectral features. The graph Laplacian is decomposed. The number of connected components and the first 5 non-zero eigenvalues are selected as the spectral graph-level features. An estimated indicator of whether a node is included in the largest connected component and the first 2 eigenvectors of the non-zero eigenvalues are selected as the spectral node-level features.

Molecule features. On molecule datasets, the valency of each atom is selected as the node-level feature, and the total weight of the whole molecule is selected as the graph-level feature.

The above node-level features and graph-level features are concatenated together as the auxiliary node-level features \mathbf{F}_{aux} and graph-level features \mathbf{y} . An important property is that the above node-level features are permutation-equivariant and the above graph-level features are permutation-invariant, whose proof is straightforward so we omit it here.

PNA module. The PNA module [11] is implemented as follows,

$$\text{PNA}(\{\mathbf{x}_i\}_{i=1}^n) = \text{MLP}(\min(\{\mathbf{x}_i\}_{i=1}^n) \oplus \max(\{\mathbf{x}_i\}_{i=1}^n) \oplus \text{mean}(\{\mathbf{x}_i\}_{i=1}^n) \oplus \text{std}(\{\mathbf{x}_i\}_{i=1}^n)) \quad (74)$$

where \oplus is the concatenation operator, $\mathbf{x}_i \in \mathbb{R}^d$; \min , \max , mean , and std are coordinate-wise, e.g., $\min(\{\mathbf{x}_i\}_{i=1}^n) \in \mathbb{R}^d$.

FiLM module. FiLM [49] is implemented as follows,

$$\text{FiLM}(\mathbf{x}_i, \mathbf{x}_j) = \text{Linear}(\mathbf{x}_i) + \text{Linear}(\mathbf{x}_i) \odot \mathbf{x}_j + \mathbf{x}_j \quad (75)$$

where Linear is a single fully-connected layer without activation function and \odot is the Hadamard product.

F Supplementary Details about Experiments

F.1 Hardware and Software

We implement DISCO in PyTorch⁴ and PyTorch-geometric⁵. All the efficiency study results are from one NVIDIA Tesla V100 SXM2-32GB GPU on a server with 96 Intel(R) Xeon(R) Gold 6240R CPU @ 2.40GHz processors and 1.5T RAM.

F.2 Dataset Setup

F.2.1 Dataset Statistics

The statistics about all the datasets used in this paper are presented in Table 7, where a is the number of edge types, b is the number of node types, $|\mathbf{E}|$ is the number of edges and $|\mathbf{F}|$ is the number of nodes.

Table 7: Dataset statistics.

Name	# Graphs	Split	a	b	Avg. $ \mathbf{E} $	Max $ \mathbf{E} $	Avg. $ \mathbf{F} $	Max $ \mathbf{F} $
SBM	200	128/32/40	1	1	1000.8	2258	104.0	187
Planar	200	128/32/40	1	1	355.7	362	64.0	64
Community	100	64/16/20	1	1	74.0	122	15.7	20
QM9	130831	97734/20042/13055	4	4	18.9	28	8.8	9
MOSES	1733214	1419512/156176/157526	4	8	46.3	62	21.6	27
GuacaMol	1398213	1118633/69926/209654	4	12	60.4	176	27.8	88

⁴<https://pytorch.org/>

⁵<https://pytorch-geometric.readthedocs.io/en/latest/>

F.2.2 Detailed Settings on Plain Graph Datasets

Dataset Split. We follow the settings of SPECTRE [43] and DiGress [62] to split the SBM, Planar [43], and Community [68] datasets into 64/16/20% for training/validation/test set.

Metrics. The Maximum Mean Discrepancy (MMD) [68] measures the discrepancy between two sets of distributions. The relative squared MMD [62] is defined as follows

$$score = \frac{\text{MMD}^2(\{\mathcal{G}\}_{\text{gen}} || \{\mathcal{G}\}_{\text{test}})}{\text{MMD}^2(\{\mathcal{G}\}_{\text{train}} || \{\mathcal{G}\}_{\text{test}})}, \quad (76)$$

where $(\{\mathcal{G}\}_{\text{gen}}$, $(\{\mathcal{G}\}_{\text{train}}$, and $(\{\mathcal{G}\}_{\text{test}}$ are the sets of generated graphs, training graphs, and test graphs, respectively. We report the above relative squared MMD for degree distributions (Deg.), clustering coefficient distributions (Clus.), and average orbit counts (Orb.) statistics (the number of occurrences of all substructures with 4 nodes), which are standard metrics [68] for unattributed graphs in Table 1.

In addition, the Uniqueness, Novelty, and Validity are chosen. Uniqueness reports the fraction of the generated nonisomorphic graphs; Novelty reports the fraction of the generated graphs not isomorphic with any graph from the training set; Validity checks the fraction of the generated graphs following some specific rules. For the SBM dataset, we follow the validity check from [43] whose core idea is to check whether real SBM graphs are statistically indistinguishable from the generated graphs; for the Planar dataset, we check whether the generated graphs are connected and are indeed planar graphs. Because the Community dataset does not have the Validity metric, we only report the Uniqueness, Novelty, and Validity results on the SBM and Planar datasets.

F.2.3 Detailed Settings on Molecule Graph Datasets

Dataset Split. We follow the split of QM9 from DiGress [62] and follow the split of MOSES [50] and GuacaMol [5] according to their benchmark settings. Their statistics are presented in Table 7.

Metrics. For QM9, Uniqueness, Novelty, and Validity are chosen as metrics. The first two are the same as introduced in Section F.2.2. The Validity is computed by building a molecule with Rdkit ⁶ and checking if we can obtain a valid SMILES string from it.

For MOSES, the chosen metrics include Uniqueness, Novelty, Validity, Filters, Fréchet ChemNet Distance (FCD), Similarity to a nearest neighbor (SNN), and Scaffold similarity (Scaf), which is consistent with DiGress [62]. The official evaluation code ⁷ is used to report the performance.

For GuacaMol, the chosen metrics include Uniqueness, Novelty, Validity, KL Divergence, and Fréchet ChemNet Distance (FCD), which is consistent with DiGress [62]. The official evaluation code ⁸ is used to report the performance.

F.3 Hyperparameter Settings

Forward Diffusion Settings. As we introduced in Proposition 3.2, we tried two sets of rate matrices for the node and edge forward diffusion, so that the converged distribution is either uniform or marginal distribution. We found the marginal distribution leads to better results than the uniform distribution. Thus, the reference distribution is the marginal distribution for all the main results, except Table 6. The performance comparison between the marginal diffusion and uniform diffusion is presented in the Ablation study in Section 4.4. The $\beta(t)$ controls how fast the forward process converges to the reference distribution, which is set as $\beta(t) = \alpha\gamma^t \log(\gamma)$, which is consistent with many existing works [18, 59, 7]. In our implementation, we assume the converged time $T = 1$ and for the forward diffusion hyperparameters (α, γ) we tried two sets: (1.0, 5.0) and (0.8, 2.0) where the former one can ensure at $T = 1$ the distribution is very close to the reference distribution, and the latter one does not fully corrupt the raw data distribution so the graph-to-graph model $p_{0|t}^\theta$ is easier to train.

⁶<https://www.rdkit.org/>

⁷<https://github.com/molecularsets/moses>

⁸<https://github.com/BenevolentAI/guacamol>

Table 8: Generation performance on the Community dataset.

Model	Deg.↓	Clus.↓	Orb.↓
GraphRNN [68]	4.0	1.7	4.0
GRAN [35]	3.0	1.6	1.0
GG-GAN [30]	4.0	3.1	8.0
MolGAN [8]	3.0	1.9	1.0
SPECTRE [43]	0.5	2.7	2.0
DiGress [62]	1.0	0.9	1.0
DISCO-MPNN	1.4±0.5	0.9±0.2	0.9±0.3
DISCO-GT	0.9±0.2	0.9±0.3	1.1±0.4

Reverse Sampling Settings. The number of sampling steps is determined by τ , which is $\text{round}(\frac{1}{\tau})$ if we set the converged time $T = 1$. We select the number of sampling steps from $\{50, 100, 500\}$, which is much smaller the number of sampling steps of DiGress [62] from $\{500, 1000\}$. For the number of nodes n in every generated graph, we compute a graph size distribution of the training set by counting the number of graphs for different sizes (and normalize the counting to sum it up to 1). Then, we will sample the number of nodes from this graph size distribution for graph generation.

Neural Network Settings. For DISCO-GT, the parametric graph-to-graph model $p_{0|t}^\theta$ is graph transformer (GT)-based. We use the exactly same GT architecture as DiGress [62] and adopt their recommended configurations⁹. The reason is that this architecture is not our contribution, and setting the graph-to-graph model $p_{0|t}^\theta$ same can ensure a fair comparison between the discrete-time graph diffusion framework (from DiGress) and the continuous-time graph diffusion framework (from this work). For DISCO-MPNN, we search the number of MPNN layers from $\{3, 5, 8\}$, set all the hidden dimensions the same, and search it from $\{256, 512\}$. For both variants, the dropout is set as 0.1, the learning rate is set as $2e^{-4}$, and the weight decay is set as 0.

F.4 Additional Results on Community

Additional Community plain graph dataset results are in Table 8. Our observation is consistent with the main content: both variants of DISCO are on par with the SOTA general graph diffusion generative model, DiGress.

F.5 Convergence Study

Figure 3 shows the training loss of DISCO-GT and DISCO-MPNN on four datasets, whose X-axis is the number of iterations (i.e., the number of epochs \times the number of training samples / batch size). We found that overall the training losses converge smoothly on 4 datasets.

F.6 Visualization

The generated graphs on the SBM and Planar datasets are presented in Figure 4. We clarify that the generated planar graphs are selected to be valid because, as Table 1 shows, not all the generated graphs are valid planar graphs, but the planar layout requires it in our visualization setting¹⁰. The generated SBM graphs are not selected; even if a part of them cannot pass the strict SBM statistic test (introduced in Section F.2.2 - Metrics), most, if not all, of them still form 2 – 5 densely connected clusters.

The generation trajectory of SBM graphs is presented in Figure 5 which demonstrates the reverse denoising process visually.

⁹<https://github.com/cvignac/DiGress/tree/main/configs/experiment>

¹⁰https://networkx.org/documentation/stable/reference/generated/networkx.drawing.layout.planar_layout.html

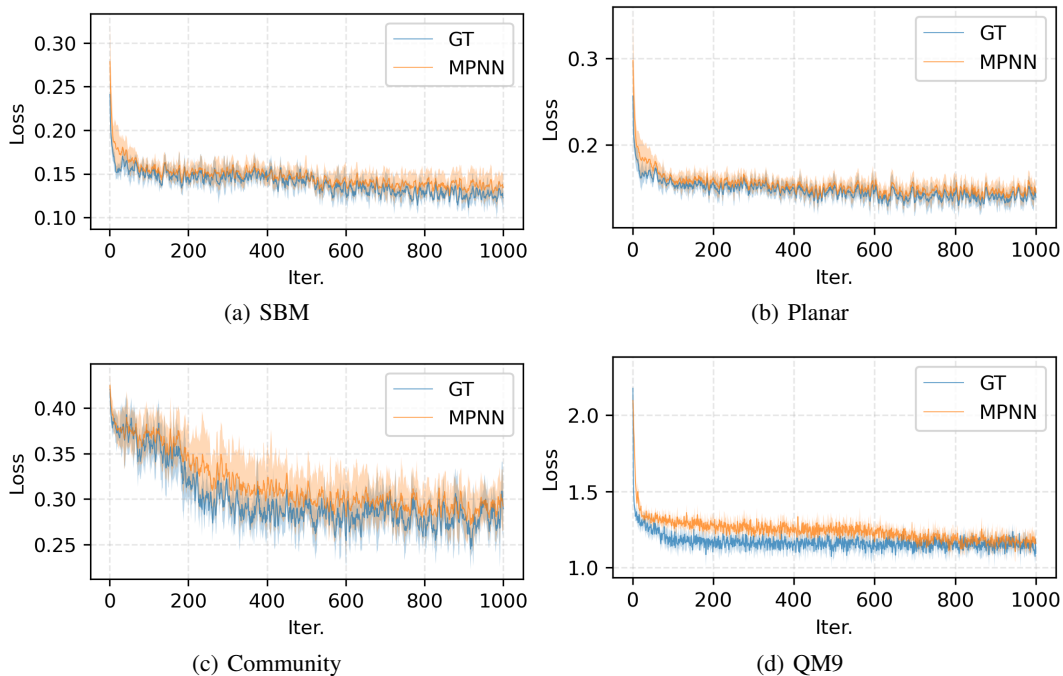
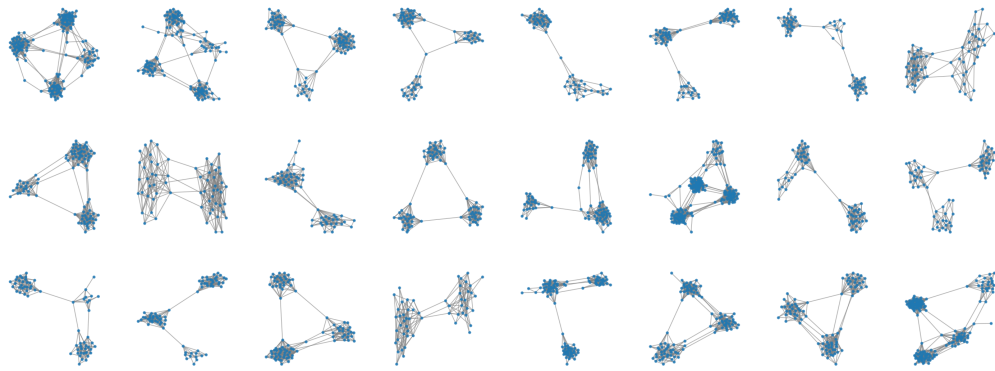


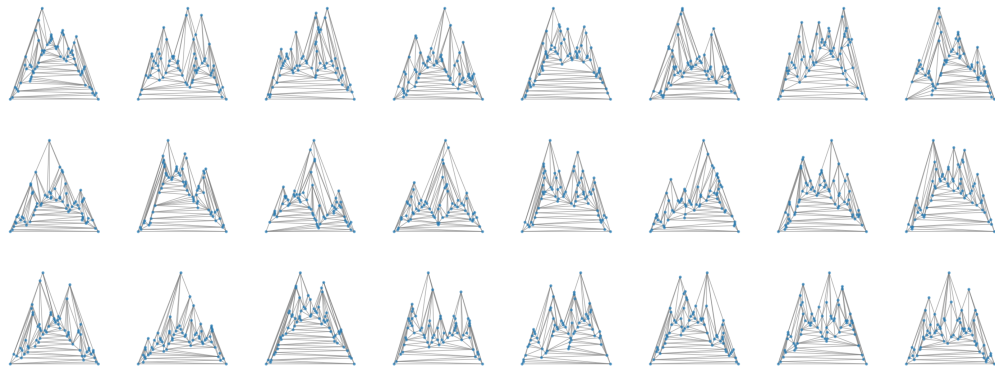
Figure 3: Training loss of DISCO on different datasets and backbone models.

G Limitation and Future Work

In this paper, we study the generation of graphs with categorical node and edge types. The current model DISCO cannot be applied to generate graphs with multiple node/edge features (e.g., multiplex networks) and this is an important future work to study. Also, we view the absence of edge as a special type of edge, which forms a complete graph and promotes the expressiveness of our MPNN backbone model. However, it will lead to quadratic complexity concerning the number of nodes. For our current dataset (e.g. graphs with < 1000 nodes) the complexity is still acceptable. However, for future studies on generating large graphs, we aim to design more efficient diffusion generative models.



(a) SBM



(b) Planar

Figure 4: Generated graphs.

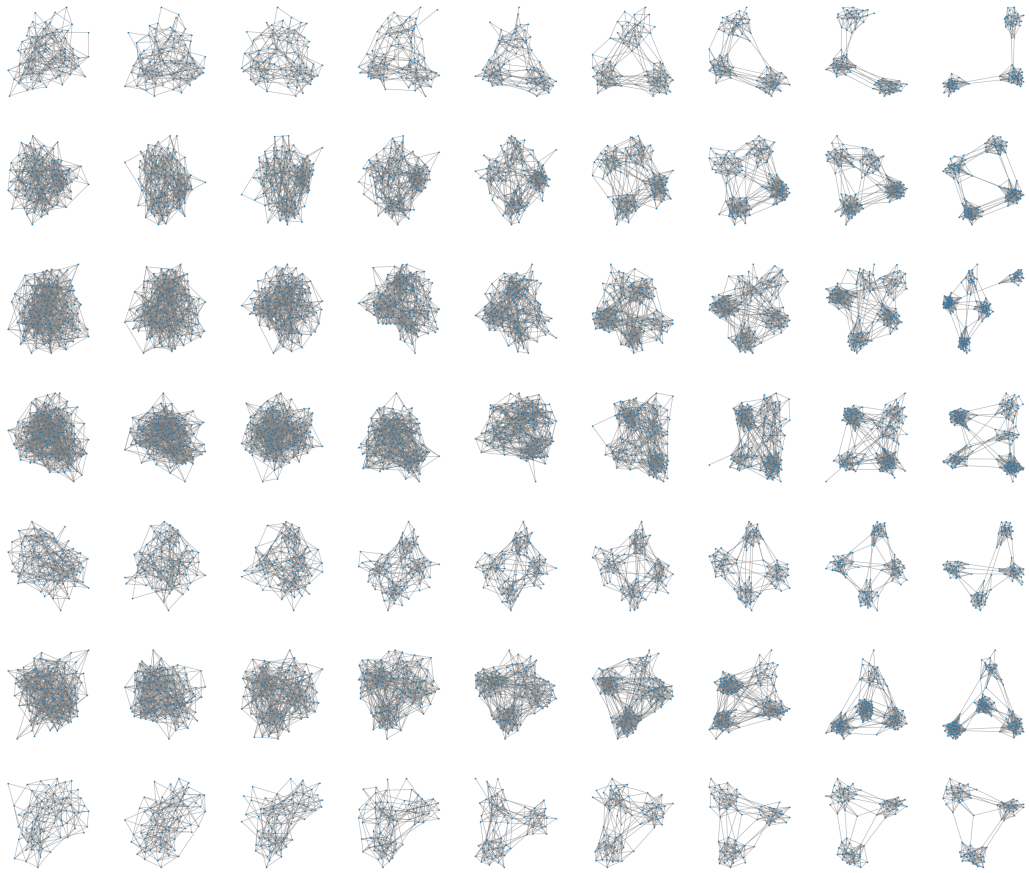


Figure 5: Generation trajectory of SBM graphs with different sizes. Every row is the generation trajectory of one graph from time $t = T$ (left) to $t = 0$ (right) with equal time intervals.